Quantifying the Influence of the Sea Surface Temperature Pattern Effect on Transient Global Warming

ROBIN GUILLAUME-CASTEL[a,b,c] AND BENOIT MEYSSIGNAC[a]

[a] *LEGOS, Université de Toulouse, CNRS/CNES/UPS/IRD, Toulouse, France*
[b] *Geophysical Institute, University of Bergen, Bergen, Norway*
[c] *Bjerknes Center for Climate Research, Bergen, Norway*

(Manuscript received 25 April 2024, in final form 19 March 2025, accepted 7 April 2025)

ABSTRACT: The pattern of surface warming plays a significant role in Earth's response to radiative forcing as it influences climate feedbacks. Distinct patterns of surface warming lead to different equilibrium and transient responses to identical forcing, emphasizing the need to analyze this pattern effect. While existing studies have primarily focused on assessing the influence of surface warming patterns on long-term warming (equilibrium climate sensitivity, committed warming), their role in the transient global warming remains partially understood. Here, we introduce a novel analytical method to quantify the influence of the pattern effect on transient global warming. We use an energy budget which explicitly separates the radiative response caused by uniform global surface warming from the response induced by changing surface temperature patterns. Using this new energy balance model, we assess the relative contribution of the radiative response induced by changing surface temperature patterns to global warming in idealized forcing experiments (1pctCO_2) from 12 CMIP6 models. We show that the pattern effect consistently dampens global warming in 9 out of 12 models at decadal time scales. We specifically quantify that the pattern effect induces a change in the transient climate response of −6.0% [−11.3%; 0.5%] (mean and quantiles 17–83) compared to a scenario where the warming pattern is uniform. Our study demonstrates that distinct models exhibit significantly different transient global warming with differences being amplified by variations in the pattern effect. Overall, our results highlight the importance of changing warming patterns, through the pattern effect, in influencing decadal-scale transient warming. These findings support recent suggestions to incorporate warming pattern uncertainties in future climate projections.

KEYWORDS: Sea surface temperature; Climate change; Climate sensitivity; Feedback; Radiation budgets

1. Introduction

Understanding what causes changes in global mean surface temperature (GMST) is one of the most critical aspects of climate change science as GMST changes play a key role in Earth's energy budget. GMST is also a key driver of regional climate change and associated impact drivers. Indeed, the pattern of many variables, such as surface temperature, ocean heat content, sea level change, precipitation extremes, and others, scales with GMST, making GMST a relevant index of future local changes (e.g., Santer et al. 1990; Mitchell 2003; Perrette et al. 2013; Grose et al. 2017).

GMST changes are governed by Earth's energy budget both at the top of the atmosphere (TOA) and at the surface (Archer and Pierrehumbert 2011). In recent decades, growing evidence has highlighted how the response of the TOA energy budget to increasing radiative forcing is intricately linked to surface warming patterns through their radiative effect (Andrews et al. 2015; Armour et al. 2013), a phenomenon usually referred to as the "pattern effect" (Stevens et al. 2016; IPCC 2021). In particular, the tropical Pacific temperature gradient between the Indo-Pacific warmpool to the west and the cold tongue to the east has been shown to affect the Pacific Walker circulation, a process associated with changes in the low cloud amount in subsidence areas in the eastern Pacific. As a result, the cloud radiative effect is changed, leading to substantial changes in the TOA energy budget (Andrews and Webb 2018; Ceppi and Gregory 2017; Schiro et al. 2022; Zhou et al. 2017).

Long-term warming, such as the equilibrium climate sensitivity (ECS), or the committed warming, is significantly affected by these warming patterns (Andrews et al. 2018, 2022; Armour 2017; Dong et al. 2021; Marvel et al. 2018; Sherwood et al. 2020; Zhou et al. 2021). More specifically, Dong et al. (2021) showed that the effective climate sensitivity estimated from CMIP5 abrupt-4xCO_2 simulations was on average 2.3 K higher than estimated with historical observations. This difference was mainly attributed to the pattern effect. In addition, Zhou et al. (2021) estimated that current committed warming would increase from 1.3 to 2 K if observed warming patterns transitioned to the warming patterns simulated in abrupt-4xCO_2 simulations.

Similarly, other studies have focused on the influence of the pattern effect on transient global warming and how it could influence climate projections (Geoffroy et al. 2013b, 2012; Alessi and Rugenstein 2023; Frey et al. 2017; Watanabe et al. 2021; Dong et al. 2021; Armour et al. 2024). Geoffroy et al. (2012)

Denotes content that is immediately available upon publication as open access.

Supplemental information related to this paper is available at the Journals Online website: https://doi.org/10.1175/JCLI-D-24-0229.s1.

Corresponding author: Robin Guillaume-Castel, robin.guillaume-castel@uib.no

DOI: 10.1175/JCLI-D-24-0229.1

notably quantified the influence on transient warming of the ocean heat uptake efficacy, a quantity that can be representative of the pattern effect (Geoffroy et al. 2013b; Winton et al. 2013). They estimated that, in CMIP5 models, the ocean heat uptake efficacy reduces the transient climate response (TCR, a common metric used to quantify transient warming) by 0.3 ± 0.3 K, which corresponds to approximately 15% of the total TCR. Using a subset of CMIP6 models, Dong et al. (2021) quantified that the TCR estimated from historical simulations was on average 13% smaller than estimated with 1pctCO_2 simulations, mostly because of the pattern effect. More recently, other studies (Alessi and Rugenstein 2023; Watanabe et al. 2021; Dong et al. 2022; Armour et al. 2024) have shown that changing warming patterns could introduce uncertainties in global climate projection. More specifically, Alessi and Rugenstein (2023) determined that the pattern effect could increase the total model uncertainty by 40% for global climate projections of surface temperature. They additionally quantified that, for one model, the pattern effect could increase global surface warming by up to 1 K in the scenario RCP8.5. Similarly, Watanabe et al. (2021) quantified that the pattern effect could amplify global warming by 9%–30% in climate projections for different scenarios. In addition, Armour et al. (2024) showed that the peculiar observed warming patterns have slowed down global warming over recent decades. A more uniform warming would have led to an increased global warming rate.

Overall, these different studies have highlighted how understanding the influence of the pattern effect on transient warming is critical for understanding global warming and for accurate climate projections. While multiple frameworks have been proposed to determine how the pattern effect modifies long-term warming, relatively few attempts have been made to quantify its impact on transient global warming. This paper introduces a novel framework allowing to analytically determine the influence of the pattern effect on global transient warming across the entire time series.

We introduce a novel approach that employs a recently developed multivariate energy balance model (Meyssignac et al. 2023b) to quantify the influence of the pattern effect on transient warming. By explicitly separating the contributions of uniform global surface warming from the contribution of changing warming patterns to Earth's radiative response, we develop a relevant framework for quantifying and interpreting the impact of the pattern effect on transient global warming. Section 2 outlines the development of the multivariate energy balance model and its application in assessing the GMST change attributable to the pattern effect. Section 3 describes the data and methodology employed to evaluate the pattern effect and its impact on global warming in climate model simulations. In section 4, we detail our findings, followed by a discussion in section 5 that explores the implications of our results and the limitations of our approach. The paper concludes with a summary of our key insights in section 6.

2. Analytical decomposition of the radiative response of Earth

We assume that the preindustrial climate is in a dynamical steady state. From there, the radiative forcing change induced by increasing the atmospheric concentration of carbon dioxide F causes a global energy imbalance N. In response to this imbalance, the surface temperature of Earth changes, gradually increasing the radiative response of Earth R to compensate for the imbalance induced by the increasing atmospheric concentration of carbon dioxide. Earth's energy budget reads

$$N(t) = F(t) + R(t). \tag{1}$$

A common approach is to consider that the radiative response change R only depends on the GMST anomaly T through a multiplicative constant λ, usually called the climate feedback parameter (Budyko 1969; Sellers 1969; North and Kim 2017). The climate feedback parameter is derived from a Taylor expansion of $R(T)$. While the pattern effect has often been interpreted as a time-dependent climate feedback parameter $\lambda(t)$ (Armour et al. 2013; Dong et al. 2019; Wills et al. 2021; Meyssignac et al. 2023a), we follow a different approach which consists in explicitly separating the contribution of the GMST and of changing warming patterns to the radiative response beforehand, to account for the apparent time variations in the climate feedback parameter [we refer the reader to Meyssignac et al. (2023b) for a detailed description and comparison between the two approaches].

The key hypothesis is that the radiative response of Earth depends not only on the GMST change $\overline{T}(t)$ (the overbar denotes a global mean quantity) but also on changes in the pattern of surface warming, denoted as $T'_x(t)$, that we define as the distance of local surface warming to global mean surface warming. By explicitly separating these two dependencies, the change in radiative response R, which follows the increased radiative forcing F, can be written using a first-order Taylor expansion with regard to these different variables (Zhang et al. 2023; Bloch-Johnson et al. 2024; Meyssignac et al. 2023b):

$$R(t) = \frac{\partial R}{\partial \overline{T}}\overline{T}(t) + \sum_x \frac{\partial R}{\partial T'_x} T'_x(t), \tag{2}$$

where x stands for the locations on the globe. Here, the radiative response is separated into two different terms. The first term corresponds to the radiative response to changes in GMST. The value of $\partial R/\partial \overline{T}$ corresponds to the magnitude of the net climate feedback if the warming is uniform. We denoted this term as λ_u, corresponding to a uniform warming climate feedback parameter. The second term corresponds to the radiative response to the changes in the surface temperature patterns with no changes in the GMST. In other words, this term represents the pattern effect. Note that, while it is more common to study the pattern effect relative to equilibrated warming (e.g., Dong et al. 2022; Sherwood et al. 2020; Andrews et al. 2018, 2022), a few recent studies follow an approach similar to ours by comparing a given pattern to uniform warming (Zhang et al. 2023; Bloch-Johnson et al. 2024; Meyssignac et al. 2023b). The term *pattern effect* in this paper designates the second term here, which is the radiative response to nonuniform warming, and we denote it as P. For simplicity, $\partial R/\partial T'_x$ is denoted as η_x for a given x such that

$P = \sum_x \eta_x T'_x(t)$. This multivariable approach is, in essence, similar to other studies where the radiative response to uniform warming is separated from the radiative response to changing warming patterns, either explicitly (Zhou et al. 2016; Gregory et al. 2020) or through an additional variable in the global energy budget (e.g., Ceppi and Gregory 2019; Fueglistaler 2019).

Incorporating the radiative response decomposition [Eq. (2)] in the global Earth energy budget [Eq. (1)] leads to

$$N(t) = F(t) + \lambda_u \overline{T}(t) + P(t). \tag{3}$$

To determine the influence of the pattern effect on the GMST change, we use the following simple two-layer diffusion model for ocean heat uptake (Dickinson 1981; Gregory 2000; Raper et al. 2002; Held et al. 2010; Geoffroy et al. 2013a; North and Kim 2017; Rohrschneider et al. 2019):

$$\begin{cases} C\dfrac{d\overline{T}}{dt} = F(t) + \lambda_u \overline{T}(t) + P(t) - \gamma(\overline{T} - \overline{T}_0) \\ C_0\dfrac{d\overline{T}_0}{dt} = \gamma(\overline{T} - \overline{T}_0) \end{cases}, \tag{4}$$

where C and C_0 are the heat capacities of the surface layer and of the deep ocean layer, respectively; γ is the diffusion heat exchange coefficient between the two layers; and $\overline{T}_0$ is the temperature change of the deep ocean layer. By construction, the variable P represents higher moments of the surface temperature distribution than $\overline{T}$, which means P can be considered mostly independent from $\overline{T}$.

In Eq. (4), the pattern effect acts as a pseudoforcing (Zhou et al. 2021), which contributes to the GMST change the same way that the radiative forcing does. As a consequence, the surface GMST change can be written as the sum of two contributions: the GMST response to the radiative forcing that we denote it as $\overline{T}_F$ and the GMST response to the pattern effect that we denote it as $\overline{T}_P$. Similarly, the deep ocean temperature can also be written as the sum of two contributions $\overline{T}_{0F}$ and $\overline{T}_{0P}$. The two-layer energy budget now reads

$$\begin{cases} \overline{T}(t) = \overline{T}_F(t) + \overline{T}_P(t) \\ \overline{T}_0(t) = \overline{T}_{0F}(t) + \overline{T}_{0P}(t) \\ C\dfrac{d\overline{T}_F}{dt} - \lambda_u \overline{T}_F(t) + \gamma(\overline{T}_F - \overline{T}_{0F}) = F(t) \\ C_0\dfrac{d\overline{T}_{0F}}{dt} - \gamma(\overline{T}_F - \overline{T}_{0F}) = 0 \\ C\dfrac{d\overline{T}_P}{dt} - \lambda_u \overline{T}_P(t) + \gamma(\overline{T}_P - \overline{T}_{0P}) = P(t) \\ C_0\dfrac{d\overline{T}_{0P}}{dt} - \gamma(\overline{T}_P - \overline{T}_{0P}) = 0 \end{cases}. \tag{5}$$

Solving Eq. (5) [following the same approach as Geoffroy et al. (2013a), Rohrschneider et al. (2019)] yields an analytical expression of the time changes in the GMST response to the radiative forcing and of the GMST response to the pattern effect. At a given time t, they read

$$\begin{cases} \overline{T}_F(t) = \dfrac{1}{C(\psi_s + \psi_f)}\left[\psi_f \displaystyle\int_0^t F(s)e^{-(t-s)/\tau_f}ds + \psi_s \int_0^t F(s)e^{-(t-s)/\tau_s}ds\right] \\ \overline{T}_P(t) = \dfrac{1}{C(\psi_s + \psi_f)}\left[\psi_f \displaystyle\int_0^t P(s)e^{-(t-s)/\tau_f}ds + \psi_s \int_0^t P(s)e^{-(t-s)/\tau_f}ds\right] \end{cases}, \tag{6}$$

where τ_s and τ_f are the slow and fast characteristic times, respectively, and ψ_f and ψ_s are the mode parameters [see appendix A and Geoffroy et al. (2013a), Rohrschneider et al. (2019) for more details].

Equation (6) suggests the GMST response to the pattern effect has the same temporal structure as the response to the forcing. They both show two characteristic time scales associated with the atmospheric and surface feedback strength (represented by λ_u) and with the vertical heat transport in the ocean (represented by the parameters C, C_0, and γ). The first time scale corresponds to an interannual to decadal response ($\tau_f \sim$ 1–3 years in climate models), while the second time scale represents the multidecadal to centennial response [$\tau_s \sim$ 100 years in climate models, Smith et al. (2021)].

3. Data and methods

In this section, we quantify each term of the multivariate energy budget [Eq. (3)] in 1pctCO_2 simulations from different climate models. We separately compute the radiative response induced by a uniform warming, the pattern effect, and the radiative forcing. Using these estimates, we validate the multivariable energy balance model introduced in section 2 by checking that the global energy budget is closed in climate model simulations. We then use Eq. (6) to quantify the global mean surface temperature change induced by the pattern effect in 1pctCO_2 simulations ran with climate model.

a. Data used in this study

To evaluate the transient warming in response to increasing CO_2 concentrations, we choose to approach the problem using idealized simulations from the latest generation of coupled climate models: CMIP6 (Eyring et al. 2016). The 1pctCO_2 experiment allows to simulate transient warming similar to what has been experienced in the twentieth century and what is expected to happen in the twenty-first century. In these simulations, carbon dioxide concentrations are increased at a rate of 1% per year from the preindustrial concentration, leading to a doubling in the CO_2 concentration after 70 years and a quadrupling after 140 years. This experiment is notably used to quantify a commonly used climate metric that is representative of transient warming: the TCR (IPCC 2021). The TCR is the GMST change reached after 70 years of the 1pctCO_2 experiment and is usually considered representative of warming in the next century (Grose et al. 2018). In this paper, we study the influence of the pattern effect not only on the time-dependent transient GMST change but also on the TCR.

To determine λ_u, our analysis requires models to be run with uniform warming experiments. Such experiments (notably amip-p4K, amip-m4K, and piSST-pxK) are part of the

Cloud Feedback Model Intercomparison Project (CFMIP; Webb et al. 2017). Overall, 13 models were run with amip-p4K experiments, nine with amip-m4K and four with piSST-pxK. Out of the 13 models, only one (TaiESM1) was not usable because of missing data on ESGF, where CMIP data are stored.

To compute the pattern effect, we use Green's functions (GFs), which are extensively detailed in Bloch-Johnson et al. (2024). The GFs are based on hundreds of climate model simulations, which are combined to provide an estimate of the radiative response to a localized anomaly of sea surface temperature. Ideally, we should use each of the individual GF of all 12 CFMIP models. However, at the moment, six GFs are readily available online, and only two models are within the 12 CFMIP models selected. To conduct a multimodel analysis, we use all 12 CFMIP models combined with the six GFs. The models used and their corresponding references are presented in Table 1.

b. *Quantifying the radiative response induced by uniform warming*

In our framework, the uniform warming climate feedback parameter λ_u is assumed to be an AOGCM-specific constant that depends on the response of the atmosphere to surface warming. To determine such quantity, we use pairs of forced atmospheric simulations with similar boundary conditions, except that an additional, spatially uniform surface temperature anomaly is prescribed in one of the two simulations [usually referred to as "Cess experiments" (Cess et al. 1990)]. Within CMIP6, three such pairs exist, namely, amip-p4K and amip, amip-m4K and amip, and piSST-pxK and piSST. When comparing two experiments in a given pair, both the radiative forcing and the pattern of surface temperature are identical as the simulations only differ by global mean surface temperature. Therefore, subtracting the global energy budget [Eq. (3)] from one experiment to another leads to

$$N_2(t) - N_1(t) = \lambda_u[\overline{T}_2(t) - \overline{T}_1(t)]. \tag{7}$$

From this equation, we deduce λ_u by dividing the temporal averages (represented by $\langle\cdot\rangle$) of both terms by the GMST difference:

$$\lambda_u = \frac{\langle N_2(t) - N_1(t)\rangle}{\langle \overline{T}_2(t) - \overline{T}_1(t)\rangle} = \frac{\langle \Delta N(t)\rangle}{\langle \Delta \overline{T}(t)\rangle}. \tag{8}$$

Due to the prescribed sea ice in both amip-p4K simulations and Green's function experiments, the sea ice albedo feedback is missing from the estimates of λ_u. While some studies have shown the influence on sea ice on the pattern effect (e.g., Dong et al. 2019; Andrews et al. 2018, 2022), this is not the focus of the current paper. We therefore choose to follow the simpler approach of Ceppi and Gregory (2019), where the lack of sea ice albedo feedback is corrected by adding a constant value with a relevant magnitude α_{ice} to the initial value of λ_u. The method to obtain values of α_{ice} is detailed in appendix B.

The adjusted value of λ_u can be expressed as

TABLE 1. Coupled models and Green's functions used in this study.

Coupled CMIP6 models Model	Coupled model reference
BCC-CSM2-MR	Wu et al. (2019)
CESM2	Danabasoglu et al. (2020)
CNRM-CM6-1	Voldoire et al. (2019)
CanESM5	Swart et al. (2019)
E3SM-1-0	E3SM Project (2018)
GFDL-CM4	Dunne et al. (2020)
GISS-E2-1-G	Kelley et al. (2020)
HadGEM3-GC31-LL	Williams et al. (2018)
IPSL-CM6A-LR	Boucher et al. (2020)
MIROC6	Tatebe et al. (2019)
MRI-ESM2-0	Yukimoto et al. (2019)
NorESM2-LM	Seland et al. (2020)
GF model	**Model reference/Green's function reference**
CAM4	Neale et al. (2013)/Dong et al. (2019)
CAM5	Neale et al. (2010)/Zhou et al. (2017)
CanESM5	Swart et al. (2019)/Bloch-Johnson et al. (2024)
ECHAM6	Stevens et al. (2013)/ Alessi and Rugenstein (2023)
GFDL-CM4	Zhao et al. (2018)/Zhang et al. (2023)
HadCM3	Gordon et al. (2000)/Bloch-Johnson et al. (2024)

$$\lambda_u = \frac{\langle \Delta N(t)\rangle}{\langle \Delta \overline{T}(t)\rangle} + \alpha_{\text{ice}}. \tag{9}$$

The results obtained are summarized in Table 2. The three pairs of experiments used to determine λ_u are generally consistent for a given model at the level of a tenth or two of W m^{-2} K^{-1}, with slightly more negative values obtained with amip-m4K than amip-p4K [thoroughly documented in Ringer et al. (2023)]. The value we use for λ_u corresponds to the mean value for all pairs available per model, which yields a multimodel mean of -1.29 ± 0.27 W m^{-2} K^{-1} (multimodel mean and standard deviation, $\pm$ always refers to one standard deviation). The radiative response induced by uniform warming is then computed by multiplying the GMST time series from each model by the uniform warming climate feedback parameter λ_u.

c. *Quantifying the pattern effect*

An increasingly more common way to quantify the influence of local surface temperature changes on the global radiative response is to use Green's functions (Barsugli and Sardeshmukh 2002; Dong et al. 2019; Bloch-Johnson et al. 2024; Zhou et al. 2017; Alessi and Rugenstein 2023; Zhou et al. 2023; Zhang et al. 2023; Williams et al. 2023). These functions are determined using hundreds of forced atmospheric simulations. In each simulation, a local patch of SST change is applied on top of a reference SST background state. Green's functions are then computed using the global top of atmosphere radiation budget from all of these experiments.

TABLE 2. Determining λ_u using multiple pairs of simulations.

Model	$\Delta N/\Delta\overline{T}$ W m^{-2} K^{-1} piSST-pxK	amip-p4K	amip-m4K	Mean	σ	α_{ice} K/K	λ_u W m^{-2} K^{-1}
BCC-CSM2-MR	—	−1.79	−1.85	−1.82	0.04	0.35	−1.47
CESM2	−1.53	−1.75	−1.77	−1.68	0.13	0.33	−1.35
CNRM-CM6-1	−1.45	−1.39	−1.65	−1.50	0.14	0.43	−1.07
CanESM5	—	−1.21	−1.18	−1.20	0.03	0.38	−0.81
E3SM-1-0	—	−1.56	—	−1.56	—	0.28	−1.28
GFDL-CM4	—	−1.82	−1.88	−1.85	0.04	0.45	−1.40
GISS-E2-1-G	—	−1.92	—	−1.92	—	0.22	−1.70
HadGEM3-GC31-LL	−1.31	−1.33	−1.35	−1.33	0.02	0.34	−1.00
IPSL-CM6A-LR	−1.34	−1.25	−1.53	−1.37	0.14	0.39	−0.98
MIROC6	—	−1.99	—	−1.99	—	0.42	−1.57
MRI-ESM2-0	—	−1.79	−1.85	−1.82	0.04	0.49	−1.33
NorESM2-LM	—	−1.80	—	−1.80	—	0.33	−1.47
Mean	−1.41	−1.63	−1.63	−1.65	0.07	0.37	−1.29
Standard deviation	0.10	0.27	0.26	0.26	0.05	0.08	0.27

The Green functions relate the increase in global radiative response per local SST change. The pattern effect (i.e., the radiative response change due to changing warming patterns) is then computed as

$$P(t) = \sum_x \mathrm{GF}(x)[\mathrm{SST}(x, t) - \overline{\mathrm{SST}}(t)], \tag{10}$$

where x indicates locations on the global ocean, GF(x) refers to the top of atmosphere radiation budget Green's function corresponding to the location x, SST(x, t) is the local SST change at the location x, and $\overline{\mathrm{SST}}$ is the global mean SST change.

Green's functions are specific to each atmospheric model used. Ideally, we should use each model's own Green's functions to compute the quantity $P(t)$. As of today, only six Green's functions are freely available online (see Table 1). They are presented in Fig. S1 in the online supplemental material. As shown in Fig. S1, and in Green's Functions Model Intercomparison Project (GFMIP; Bloch-Johnson et al. 2024), Green's functions are generally consistent between models, highlighting the same key regions, notably the warm-pool region in the tropical western Pacific and the tropical Atlantic to be responsible for most of the pattern effect. Although the exact limits of the important regions and the magnitude of the Green functions slightly differ from one model to another, we will assume that using Green's functions from these six models allows for a first-order estimate of the pattern effect in all CMIP6 models. This hypothesis should be tested for each model's own Green's functions in the future.

d. *Estimating the radiative forcing and closing the global energy budget*

To validate the multivariable approach presented in section 2, we use the global energy budget [Eq. (3)] along with our estimates of the radiative response to uniform warming and of the pattern effect to estimate the radiative forcing F. We then compare our results with independent estimates of the radiative forcing using two additional simulations. The results for the radiative response to uniform warming and for the pattern effect are shown in Fig. 3 and discussed in section 4.

In 1pctCO_2 experiments, the radiative forcing is, to a very good approximation, linear with time, as CO_2 forcing increases logarithmically with concentration (Myhre et al. 1998; Romps et al. 2022). Therefore, there is an AOGCM-specific constant f such as

$$F(t) = f \times t, \tag{11}$$

which leads to the following energy budget, when included in Eq. (3):

$$N(t) = ft + \lambda_u \overline{T}(t) + P(t). \tag{12}$$

For each model, we determine the value of f by fitting $N(t) - \lambda_u \overline{T}(t) - P(t)$ as a linear function in time using ordinary least squares. Figure 1 shows the linear fit alongside $N(t) - \lambda_u \overline{T}(t) - P(t)$ for all models studied. The linear forcing approximation is a generally appropriate estimate for all models, with a maximum RMSE of 0.5 W m^{-2} (for NorESM2-LM). We find values of f of 0.063 ± 0.006 W m^{-2} yr^{-1}, which corresponds to an equivalent 4xCO_2 forcing of $F_{4x\mathrm{CO}_2} = 8.80 \pm 0.81\,\mathrm{W\,m^{-2}}$. These values are detailed in Table 3.

We now compare our results with independent estimates of the radiative forcing, when the required simulations are available. One of the commonly used methods to compute radiative forcing corresponds to using fixed-SST experiments where a specific radiative forcing is applied [following Hansen et al. (2005)]. In CMIP6, these experiments are piClim-control and piClim-4xCO_2, from the Radiative Forcing Model Intercomparison Project (RFMIP; Pincus et al. 2016). In this method, two forced atmospheric simulations are run with similar boundary conditions in sea ice and sea surface temperature. The only difference between the two is that the first simulation has preindustrial CO_2 concentrations (piClim-control), and the other has 4 times this amount (piClim-4xCO_2). We first estimate $F_{4\times\mathrm{CO}_2} = 8.00 \pm 0.43\,\mathrm{W\,m^{-2}}$ (multimodel mean and standard deviation).

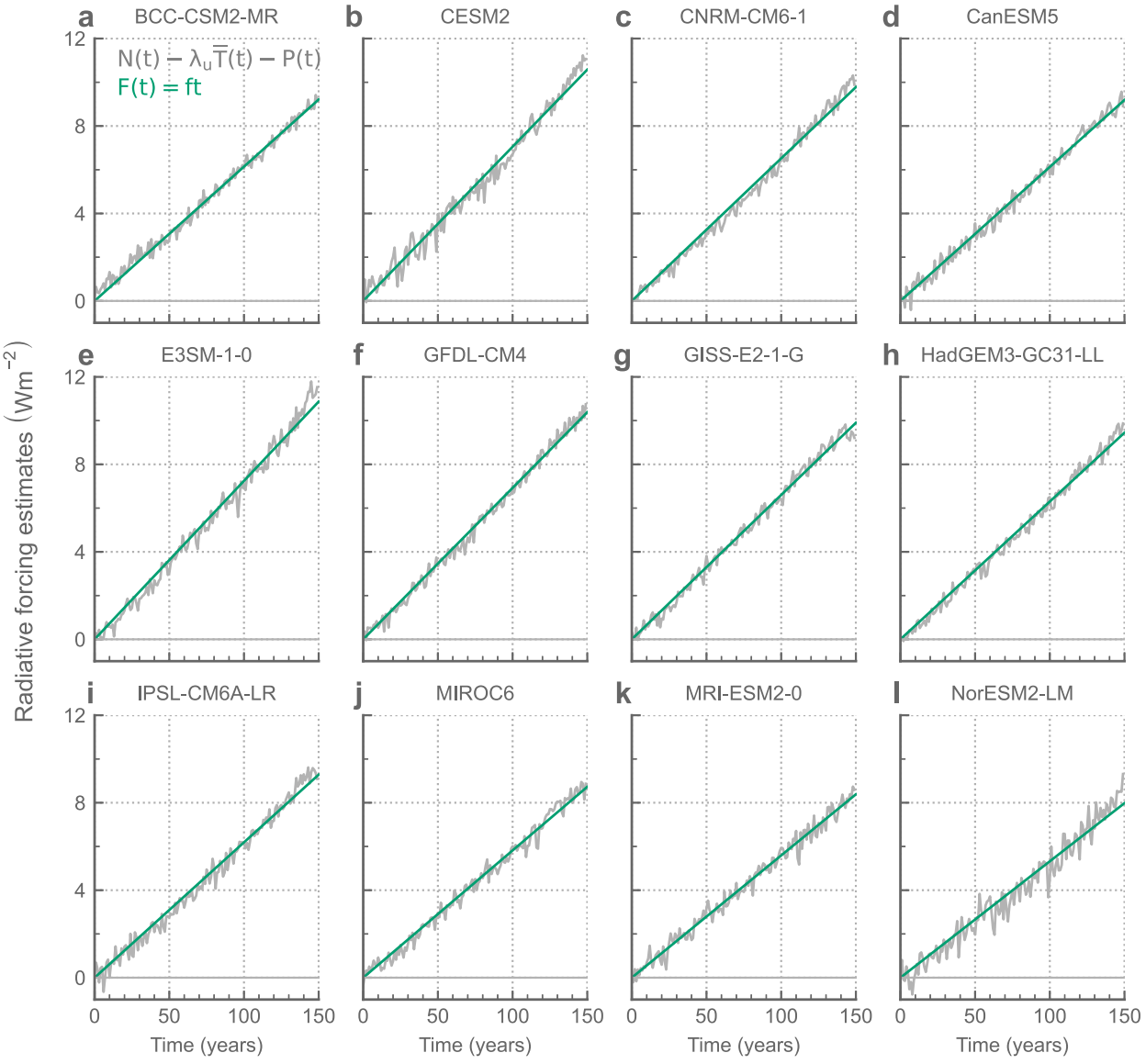

FIG. 1. Linear estimates of radiative forcing using $F(t) = ft$ (green) compared to $N(t) - \lambda_u \overline{T}(t) - P(t)$ (gray) in 1pctCO$_2$ experiments for all models studied. Overall, the linear approximation of the radiative forcing reproduces the temporal dynamics of the global energy budget.

In these experiments, while the sea surface temperature is held constant, the land temperature is allowed to vary, which can slightly affect the GMST and introduce a bias in radiative forcing estimates (Hansen et al. 2005; Forster et al. 2016; Smith et al. 2018). To account for this, following Hansen et al. (2005), we estimate the change in the radiative response caused by land warming as $\lambda_u \Delta\overline{T}$, where $\Delta\overline{T}$ represents the GMST difference between the piClim-control and piClim-4xCO$_2$ experiments. For consistency with previous applications of this method, we assume that the radiative response to uniform warming $\lambda_u \Delta\overline{T}$ is sufficient for estimating this correction (i.e., we do not account for an extra pattern effect induced by land warming). Note that for this correction, we used the estimate of λ_u before the adjustments for the sea ice albedo feedback, as sea ice is fixed in the piClim experiments. We find a $\Delta\overline{T}$ of 0.53 ± 0.06 K, which leads to an estimated error in $F_{4x\mathrm{CO}_2}$ of 0.87 ± 0.18 W m^{-2}. Overall, the fixed-SST method, corrected for land temperature warming, leads to $F_{4x\mathrm{CO}_2} = 8.88 \pm 0.52$ W m^{-2} which is consistent with our mean estimates of $F_{4x\mathrm{CO}_2}$. Individual models are compared in Fig. S2. For 8 out of 10 models tested, the two methods yield forcing estimates within 0.4 m^{-2} K^{-1}. One model (MRI-ESM2-0) shows a slightly stronger gap of 0.6 W m^{-2} K^{-1}. The last model (NorESM2-LM) shows the strongest difference 1.6 W m^{-2} K^{-1}.

Better estimates of the radiative forcing corrected for land warming could be obtained directly using experiments where

TABLE 3. Radiative forcing estimates.

Model	f (W m^{-2} yr^{-1})	(W m^{-2})			
		$F_{4\times CO_2}$ from f	piClim-4xCO_2 + land corrections	piClim-4xCO_2	land corrections
BCC-CSM2-MR	0.061	8.56	—	—	—
CESM2	0.071	9.82	9.89	8.90	0.99
CNRM-CM6-1	0.065	9.08	8.75	7.98	0.77
CanESM5	0.061	8.54	8.20	7.60	0.59
E3SM-1-0	0.072	10.10	—	—	——
GFDL-CM4	0.069	9.64	9.25	8.23	1.02
GISS-E2-1-G	0.066	9.20	9.16	7.96	1.19
HadGEM3-GC31-LL	0.063	8.78	8.79	8.08	0.71
IPSL-CM6A-LR	0.062	8.62	8.80	8.01	0.79
MIROC6	0.058	8.11	8.26	7.33	0.92
MRI-ESM2-0	0.056	7.79	8.41	7.66	0.75
NorESM2-LM	0.053	7.41	9.25	8.25	1.00
Mean	0.063	8.80	8.88	8.00	0.87
Standard deviation	0.006	0.81	0.52	0.43	0.18

both the SST and the land surface temperature are prescribed (Ackerley et al. 2018). Andrews et al. (2021) found that in one model, the forcing obtained using feedback correction, as it is done here, was 0.5 W m^{-2} K^{-1} lower than the forcing obtained with the more accurate prescribed total surface temperature. This bias could explain the differences we find in 9 out of 10 models. The stronger difference in NorESM2-LM should require more investigation.

Overall, the energy budget is closed on average over the 150 years of the 1% CO_2 simulation at the level of a few tenth of watts per square meter. To analyze more in details the closure of the energy budget, we plotted the time series of $N(t) - \lambda_u \overline{T}(t) - F(t)$ against $P(t)$, where F was estimated using piClim simulations (Fig. 2). We find that for nine models (all but for NorESM2-LM), the energy budget is closed on interannual time scales at the level of a few tenth of watts per square meter until year 80 of the 1% CO_2 simulation. For five models, it is closed for the full length of the simulation (HadGEM3-GC31-LL, CESM2, IPSL-CM6A-LR, MIROC6, and GISS-E2-1-G), while for three, it is closed until year 100 (CNRM-CM6-1, CanESM5, and GFDL-CM4).

For all models, the residuals of the energy budget [i.e., $N(t) - \lambda_u \overline{T}(t) - F(t) - P(t)$, when F is estimated with piClim simulations] evolve mostly linearly with GMST (see Fig. S3), suggesting that the remaining small residual (and even the larger error in the case of NorESM2) that is responsible for the nonclosure of the energy budget is due to a small bias in the estimate of λ_u or f or both. In some cases (e.g., CESM2, CNRM-CM6-1), these errors are not entirely linear. This could be explained by a nonlogarithmic CO_2 forcing (Gregory et al. 2015) or by a quadratic temperature dependence (Bloch-Johnson et al. 2021). This is explored in section 5 with the example of CESM2.

To summarize, using independent estimates of the uniform warming climate feedback parameter, of the pattern effect and of the radiative forcing, we reproduce the global Earth energy budget at decadal time scales within a few tenth of watts per square meter with the multivariable energy budget [Eq. (3)].

e. *Quantifying the global mean surface temperature change induced by the pattern effect*

Now that all parameters in the global energy budget [Eq. (3)] have been calculated, we calibrate the two-layer model [Eq. (4)] to determine the optimal ocean parameters C, C_0, and γ. For this purpose, we use a random draw of these three parameters based on the distributions of C, C_0, and γ from CMIP6 models, as determined by Smith et al. (2021), following the method of Geoffroy et al. (2013a). For each CMIP6 model, we perform 10 000 numerical integrations of the two-layer model, each time with a different triplet (C, C_0, and γ) from the random draw. The triplet that minimizes the distance between the reconstructed GMST through integration and the GMST output from the model is chosen for the values of the ocean parameters.

For all CMIP6 models, we find a triplet that reproduces GMST changes with a maximum RMSE of 0.16 K over the 150 years of the 1pctCO_2 experiment (see Fig. S4). The limited RMSE confirms that with consistent values of ocean parameters, the two-layer model with the multivariable energy budget accurately reproduces the temporal evolution of the global mean surface temperature anomaly. Detailed values of C, C_0, and γ are provided in Table 4. As C, C_0, and γ have been determined from a random draw within their assessed ranges in CMIP6 (Geoffroy et al. 2013a; Smith et al. 2021), they are consistent with the previously published estimates.

4. Results

a. *The pattern effect in 1pctCO_2 simulations*

The radiative response induced by nonuniform warming P is shown in Fig. 3 for each model studied. Compared to the radiative response to uniform warming, the pattern effect has less impact on the total radiative response of the planet. Indeed, P reaches mean absolute values of 0.40 ± 0.27 W m^{-2}, which is approximately 15% of the mean absolute values of

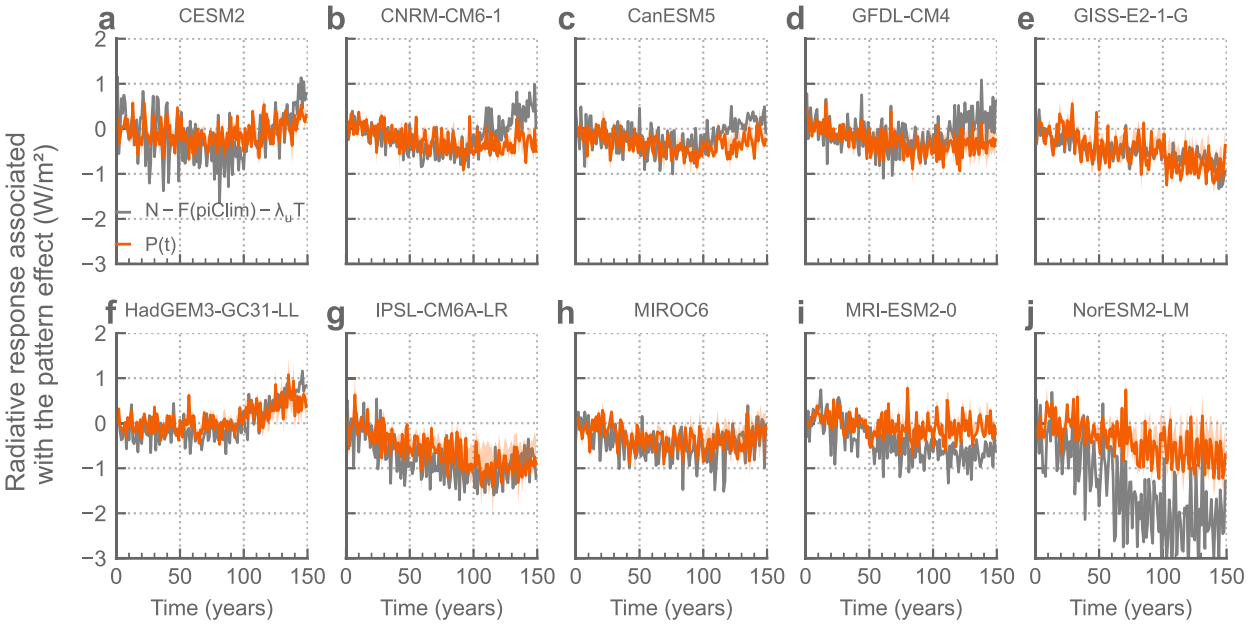

FIG. 2. Time series of the radiative response associated with the pattern effect estimated from Green functions P (red) and from the residual of the global energy budget as $N - F - \lambda_u$, where F is estimated from piClim simulations (gray).

the radiative response induced by uniform warming of 3.01 ± 0.54 W m^{-2}.

In all models, the pattern effect shows significant changes at multidecadal time scales, along with high-frequency variability at annual to decadal time scales. The time series diagnosed for each Green's function are shown in Fig. S5. In Fig. S5, we show that the different Green's functions are generally consistent qualitatively, although some quantitative differences exist. Notably, CAM4 (orange curves in Fig. S5) yields results mostly outside of the range of the other models, with almost systematically the strongest magnitudes of the pattern effect. This can be explained by CAM4's extreme sensitivity to changes in warmpool temperature (see Fig. S1). Note that CAM4 is the only model where only positive anomaly patches have been used to compute the Green functions, while other models combine positive and negative patches. Positive patches tend to lead to more sensitive Green's functions [see Fig. 2 in Bloch-Johnson et al. (2024)], which could explain why CAM4 is more sensitive than the other models.

b. *Multidecadal response*

Our results show that nonuniform warming generally amplifies the negative radiative response induced by uniform warming. In 9 out of 12 models (all but E3SM-1-0, HadGEM3-GC31-LL, and MRI-ESM2-0), the pattern effect induces a negative radiative response for most of the simulation, excluding

TABLE 4. Ocean parameters for the two-layer model for each model studied. The RMSE corresponds to the error of the GMST from the integration compared with the simulated GMST.

Model	C W m^{-2} K^{-1} yr	C_0 W m^{-2} K^{-1} yr	γ W m^{-2} K^{-1}	RMSE K
BCC-CSM2-MR	5.82	86.69	0.67	0.09
CESM2	8.20	67.03	1.02	0.13
CNRM-CM6-1	8.20	67.03	1.02	0.18
CanESM5	8.77	51.75	0.77	0.11
E3SM-1-0	9.06	28.32	0.79	0.14
GFDL-CM4	9.44	56.03	0.85	0.10
GISS-E2-1-G	10.08	121.43	0.75	0.16
HadGEM3-GC31-LL	7.89	40.05	0.95	0.11
IPSL-CM6A-LR	7.83	36.68	0.95	0.16
MIROC6	8.11	76.03	1.11	0.15
MRI-ESM2-0	7.16	135.96	0.99	0.10
NorESM2-LM	8.27	73.40	1.00	0.15
Mean	8.24	70.03	0.91	0.13
Standard deviation	1.09	32.49	0.14	0.03

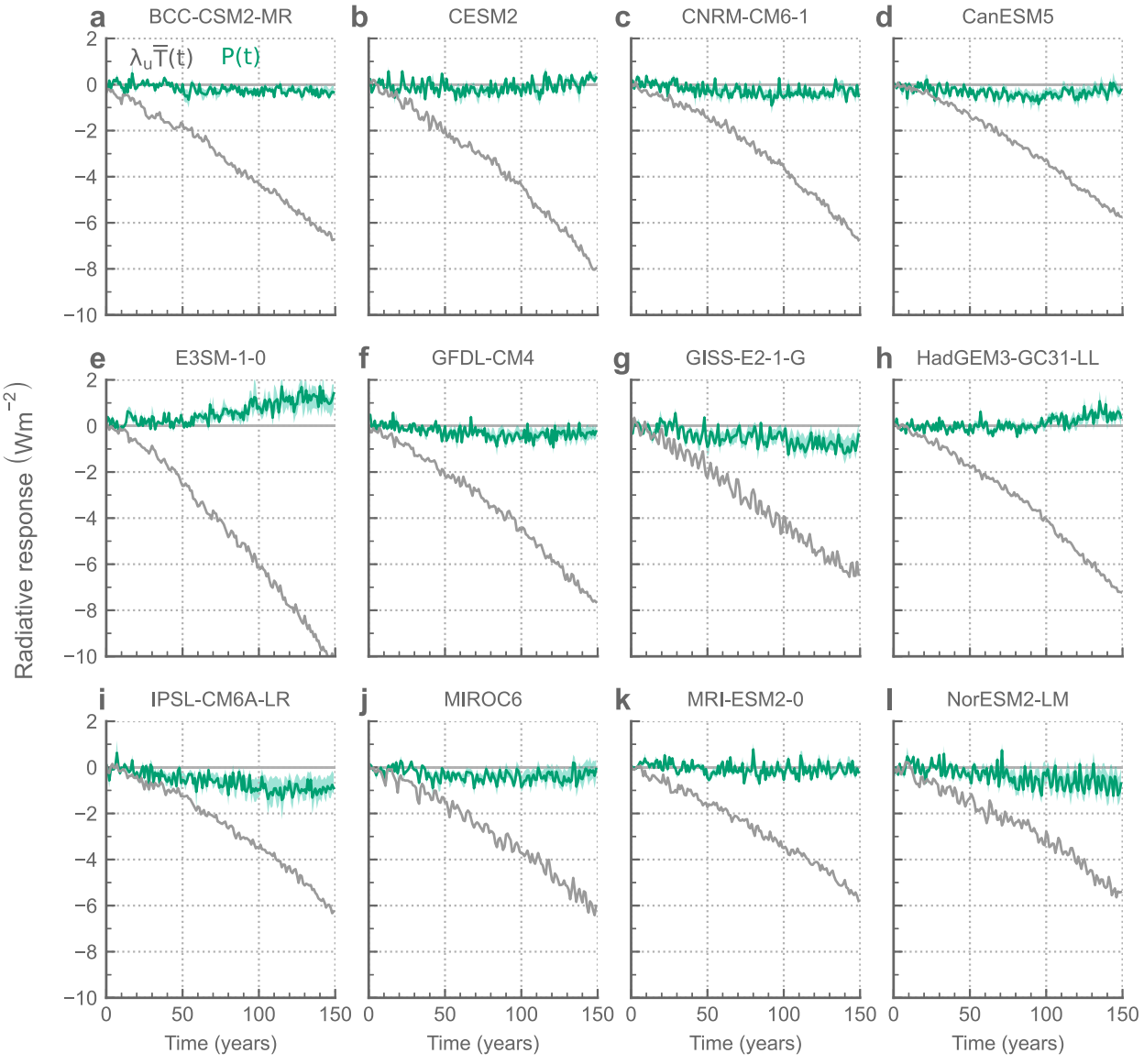

FIG. 3. Annual means of the radiative response to uniform surface warming (gray) and to changing surface warming patterns with zero-mean change (i.e., pattern effect; green) in the 1pctCO_2 experiments. The green lines for the pattern effect represent the mean values obtained with the six Green's functions. The green shaded areas represent the 17th and 83rd quantiles reached with individual Green's functions.

high-frequency variability. During the first decades of the simulation, these models show a negative trend in the pattern effect. At the minimum, the radiative response caused by the pattern effect reaches a 10-yr average of -0.53 ± 0.32 W m^{-2}. In most models, this negative trend is followed by an inflexion in the time series after 70–100 years of simulation where the pattern effect stabilizes and the trend reverses to become positive.

The radiative response caused by the pattern effect becomes positive in three models only. In this case, the pattern effect acts against the radiative response induced by uniform warming, therefore increasing the global energy imbalance. In E3SM-1-0, the pattern effect is constantly positive, with a neutral and stationary pattern effect during the first decades followed by a positive trend after 50 years of simulations. The pattern effect reaches a 10-yr average of 1.31 W m^{-2} toward the end of the simulation. In CESM2 and HadGEM3-GC31-LL, the time series inflection also yields positive values reaching 10-yr averages of 0.25 and 0.59 W m^{-2}, respectively, toward the end of the simulation.

The multidecadal change in the pattern effect is likely to be a forced response as the signal-to-noise ratio in 1pctCO_2 experiments is substantial. We verified this by computing the pattern effect in three different realizations of the 1pctCO_2 experiment using the same climate model (CanESM5; see Fig. S6). The pattern effect has the same multidecadal tendency in all three

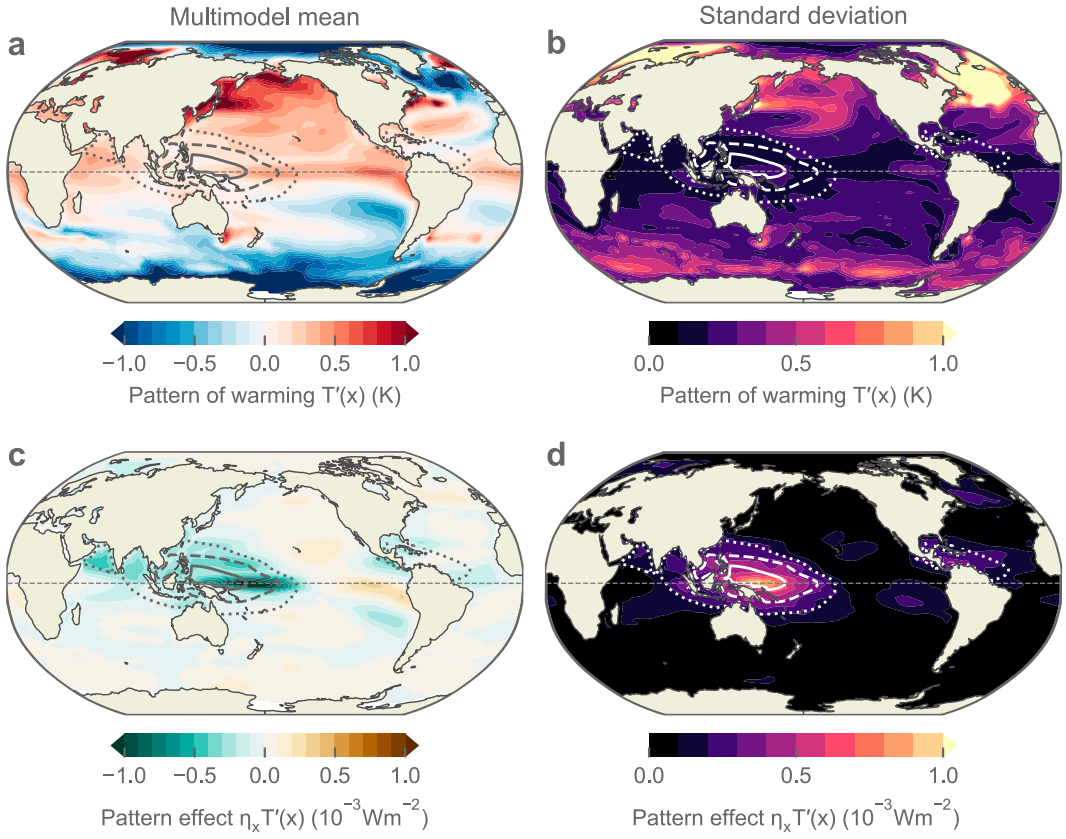

FIG. 4. (a) Multimodel mean pattern of warming at the time of doubling of carbon dioxide concentrations in 1pctCO_2 simulations, which correspond to local warming minus global warming, averaged over years 61–80 of the simulation. (b) Intermodel standard deviation of the pattern of warming. (c) Multimodel mean pattern effect at the time of doubling of carbon dioxide concentrations in 1pctCO_2 simulations, obtained by convolving the pattern of warming with the mean Green's functions. (d) Intermodel standard deviation of the pattern effect. The dotted, dashed, and plain contour lines denote the mean Green's functions contour for 1, 2, and 3 $\times$ 10^{-3} W m^{-2} K^{-1}, respectively.

realizations and only high-frequency variability is different, supporting the hypothesis of a forced signal.

To determine the regions that are responsible for this multidecadal forced signal in the pattern effect, we plot the multimodel mean and the intermodel standard deviation of the pattern of warming at the time of doubling the CO_2 in the atmosphere in 1pctCO2 simulations (averaged over years 61–80; Figs. 4a,b) and convolve these maps with the mean Green's functions, computed from the six Green's functions used in the study (Figs. 4c,d). We show that the strongest pattern values (i.e., largest deviations of local warming compared to global warming) and the strongest intermodel spread in the pattern of warming are located in high latitudes, notably in the Arctic and the Southern Ocean, but also in the North Atlantic, and the northwest Pacific. We also find that key regions where the Green functions have the most impact on the radiative response (tropical western Pacific and tropical Atlantic) show moderate patterns and very limited intermodel spread (see Figs. 4a,b).

Despite a smaller spread in warming patterns, the tropical regions have the strongest pattern effect and generate the highest intermodel standard deviation in radiative response because of the high sensitivity of the Green functions to these regions (see Figs. 4c,d). It means that differences in the pattern effect among models are governed by small differences in the pattern of warming in the key tropical regions that matter for the global energy budget.

Similar maps to Figs. 4a and 4c are presented for individual models in Figs. S7 and S8, respectively, in the supplemental material. These figures show that in the key sensitive regions of the Green functions, i.e., around the west Pacific warmpool, most models show a combination of positive, neutral, and negative radiation induced by the pattern effect. The relative weight of each contribution determines the total magnitude of the radiative response induced by the pattern effect. Meanwhile, IPSL-CM6A-LR shows an intensified warming in the entirety of the sensitive region, which leads to the strongest negative pattern effect of all the models. At the other end of the spectrum, E3SM-1-0 is the only model that shows reduced warming over the full sensitive area compared to the global average, leading to a strong positive pattern effect.

c. *Interannual and decadal internal variability*

Along with multidecadal changes, all models show internal variability at various frequencies. The pattern effect induces high-frequency internal variability of the radiative response (lower than 5 years, see Fig. 3) that could be related to the modes of internal variability that have been associated with the pattern effect such as El Niño–Southern Oscillation (ENSO; Ceppi and Fueglistaler 2021; Tsuchida et al. 2023), or the Atlantic multidecadal oscillation (AMO; Dessler 2020). The Pacific decadal oscillation (PDO) could also explain lower-frequency internal variability in the pattern effect (Loeb et al. 2018; Meyssignac et al. 2023a). As Green's functions show more sensitivity to the tropical Pacific (Bloch-Johnson et al. 2024, and Fig. S1), the internal variability here is probably more associated with ENSO and the PDO than with the AMO. Note that we do not use Green's functions for sea ice as in Bloch-Johnson et al. (2024), Dong et al. (2019), which means internal variability associated with sea ice change may be missing (Dessler 2020).

d. *Influence of the pattern effect on GMST change*

1) GLOBAL MEAN TEMPERATURE RESPONSE TO THE LONG-TERM FORCED PATTERN EFFECT

We show the results of the influence of the pattern effect on the GMST change in Fig. 5. Overall, the multidecadal changes are similar to the changes in the pattern effect, but the time series are smoothed out. As the radiative response induced by the pattern effect acts as a pseudoforcing on GMST, a negative (positive) pattern effect causes an equivalent negative (positive) forcing, which induces global cooling (warming). Most models show a damping of the warming because of the pattern effect, with cooling up to 1 K after 100 years of simulations. CESM2 shows slight cooling for the first 100 years and a slight warming amplification for the last 50 years. MRI-ESM2-0 shows no substantial change for the total simulation, while HadGEM3-GC31-LL shows no change for the first 100 years, which is followed by a warming trend until the end. E3SM-1-0 shows intensified warming because of its simulated positive pattern effect, with the strongest amplified warming of all models of up to 1 K after 150 years. The magnitude of the GMST change induced by the pattern effect can be up to 20% of the total GMST magnitude.

As presented earlier, the TCR is defined as the GMST change in response to increasing CO_2 concentrations at a rate of 1% per year until 2 times the preindustrial concentrations are reached (IPCC 2021). The TCR hence corresponds to year 70 in the 1pctO2 time series studied here. The TCR can be decomposed into two parts. The first one is directly related to the response of the global energy budget to the radiative forcing TCR_F, and the second part is the additional GMST change induced by the pattern effect TCR_P, such that

$$TCR = TCR_F + TCR_P. \tag{13}$$

For each model, we quantify TCR, TCR_F, and TCR_P by taking the average $\overline{T}$, $\overline{T}_F$, and $\overline{T}_P$ during the years 61–80 to reduce the influence of internal variability following the standard practice (e.g., Dong et al. 2021). The results are presented in Fig. 6 and Table 5. We show that the pattern effect reduces the TCR in nine out of 12 models, increases it only in one model, and does not impact it in two. On average, our results suggest that the TCR is damped by the pattern effect, with an average of −6.0% [−11.3; 0.5] (quantiles 17–83, this uncertainty includes the different Green's functions and the different coupled models).

Geoffroy et al. (2012) quantified the role of the pattern effect induced by ocean heat uptake on GMST in the transient regime. They take as a reference the "equilibrium" temperature after a doubling of CO_2 concentration (which is derived from a fit to 150 years of abrupt 4xCO_2 experiment). In addition, they assume that the pattern effect is induced by an efficacy factor ε that applies to the ocean heat uptake (Winton et al. 2010). Geoffroy et al. (2012) estimate the TCR to be around 2 K. They also estimate that the pattern effect associated with ocean heat uptake reduces the global mean surface temperature anomaly by approximately 0.25 K after 70 years of 1pctCO2 simulations (see their Fig. 1). This corresponds to a dampening of approximately 12.5% of the TCR caused by the pattern effect, which is slightly more than our estimates. This gap could be explained by three main differences between their study and ours. First, Geoffroy et al. (2012) show that the pattern effect reduces the GMST for all time scales from years 1 to 70, while in our approach, it can reduce or enhance the GMST depending on the time scale. This is because we take as a reference the preindustrial GMST, while Geoffroy et al. (2012) take as a reference the equilibrium temperature. Second, Geoffroy et al. (2012) show a monotonic response of the GMST to the pattern effect for all simulations, while, for some simulations, we show a response with an inflection point, with decreasing GMST in response to the pattern effect in the first decades and then increasing GMST in the following decades. The monotonic response in Geoffroy et al. (2012) is coming from the assumption that the pattern effect is induced by the efficacy of the ocean heat uptake. Indeed with such an assumption, the pattern effect is by definition of the same sign for all time scales in a simulation under increased CO_2 concentrations [see e.g., Fig. 4 in Winton et al. (2010)], and thus, the effect on the GMST is monotonic. Our approach, which is based on Green's functions, is more general as it allows for the pattern effect induced by any changes in the surface warming pattern and not only changes related to ocean heat uptake efficacy (see Meyssignac et al. 2023b section 7). Our approach shows that in some simulations, the surface warming pattern induces some pattern effect that leads to some inflection in the GMST response, which would not be possible if this was only driven by the global ocean heat uptake efficacy. Finally, we only use CMIP6 models, while Geoffroy et al. (2012) use models from previous CMIP generations, which could also cause differences in the results.

Overall, our analysis shows that the pattern effect generally reduces transient warming when responding to increased CO_2 forcing. Still, models show differences in the magnitude of this GMST change mediated by the pattern effect, which means that similar responses to the radiative forcing may lead

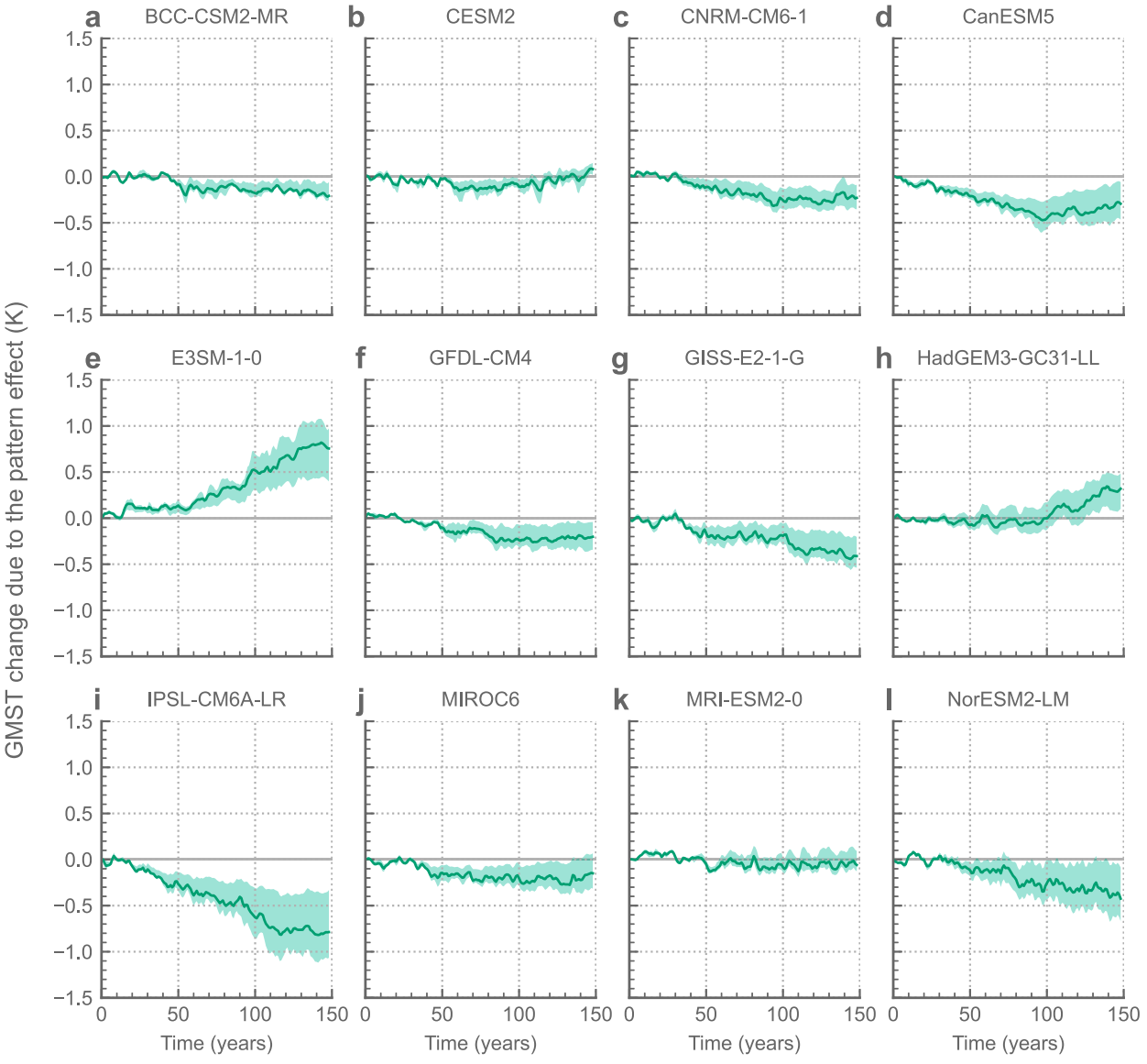

FIG. 5. GMST change induced by changing warming patterns. The lines show the results obtained with the mean pattern effect computed from the mean of Green's functions. The green shaded areas represent the 17th and 83rd quantiles reached with individual Green's functions.

to different global warming because of the pattern effect. As an example, three models studied would have a very similar TCR if the warming was uniform, but they have a different pattern effect: IPSL-CM6A-LR, HadGEM3-GC31-LL, and E3SM-1-0. Their TCR standard deviation is increased from 0.05 K with uniform warming only to 0.37 K because of the pattern effect. Our findings highlight the importance of taking the pattern effect into account when analyzing the decadal-scale GMST change in response to radiative forcing. This supports the recent claim that the pattern effect should be considered for decadal to centennial climate projections (Alessi and Rugenstein 2023; Armour et al. 2024; Watanabe et al. 2021).

2) GLOBAL MEAN TEMPERATURE RESPONSE TO THE INTERNAL VARIABILITY OF THE PATTERN EFFECT

Internal variability has a different effect on the GMST change induced by the pattern effect than on the pattern effect itself. Indeed, when integrating the radiative response of Earth to get the associated GMST changes, the ocean acts as a low-pass filter on the radiative forcing [see Eq. (5) and Geoffroy et al. (2013a)]. The ocean acts the same way on the radiative response associated with the pattern effect. This means that the high-frequency variability of the pattern effect is mostly filtered out during the integration and will not affect the GMST. The two-layer model in Eq. (5) represents this

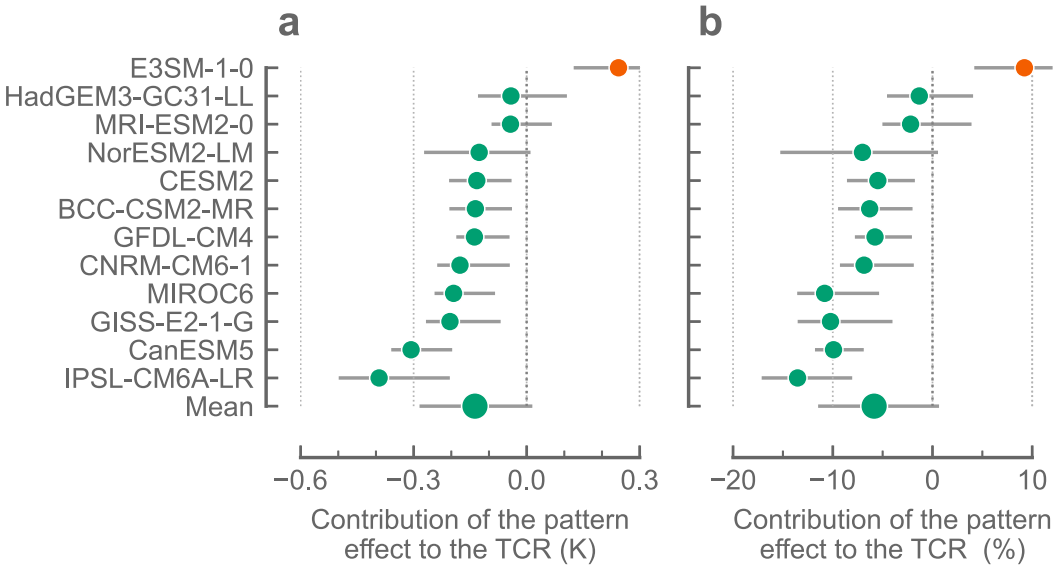

FIG. 6. Contribution of the pattern effect (green) to the TCR in (a) absolute values and (b) relative percentage. The dots represent the mean values for all the Green function, and the error bars show the 17th and 83rd quantiles. The colors represent the sign of the mean estimate.

ocean filter as a second-order low-pass filter, with a cutoff period given by

$$\tau = -2\pi\frac{\lambda_u}{C}. \tag{14}$$

We estimate this cutoff period to be 42 ± 11 years in the models studied.

The Bode plot of the two-layer model of Eq. (5) is presented in Fig. 7. It shows the magnitude of reduction and the phase shift for each period of internal variability. The high-frequency variability of the pattern effect associated, for example, with ENSO (Ceppi and Fueglistaler 2021) or sea ice changes (Dessler 2020) will be strongly attenuated and will affect the GMST change only marginally. However, lower-frequency internal variability, such as the PDO, will be hardly damped and will affect the GMST change much more intensely, although with a lag of about a quarter of the period of the low-frequency internal variability. This supports previous results from observations (Loeb et al. 2018; Meyssignac et al. 2023a).

5. Discussion

a. *Remaining errors in the multivariate energy balance model reconstruction*

In section 3, we use a multivariate energy balance model to reproduce the Earth energy imbalance as shown in Fig. 1. Although it is an appropriate approximation at multidecadal time scales, there are still some slight deviations toward the last decades of the simulations. These deviations could be explained by two different causes, which are the feedback temperature dependence and the nonlogarithmic forcing of

TABLE 5. Contribution of the radiative forcing and of the pattern effect to the TCR. Uncertainty ranges correspond to the 17th and 83rd quantiles of the values obtained with different Green's functions.

Model	TCR (K)	TCR_F (K)	TCR_P (K)	TCR_P/TCR_F (%)
BCC-CSM2-MR	1.95 [1.94; 1.96]	2.1 [2.0; 2.14]	−0.14 [−0.2; −.04]	−6.5 [−9.3; −2.2]
CESM2	2.2 [2.17; 2.23]	2.3 [2.28; 2.38]	−0.13 [−0.2; −0.04]	−5.7 [−8.4; −1.9]
CNRM-CM6-1	2.3 [2.28; 2.34]	2.5 [2.4; 2.53]	−0.18 [−0.23; −0.05]	−7.1 [−9.1; −2.0]
CanESM5	2.64 [2.63; 2.66]	3.0 [2.84; 2.99]	−0.31 [−0.35; −0.2]	−10.4 [−11.6; −7.1]
E3SM-1-0	3.06 [3.01; 3.1]	2.8 [2.72; 2.97]	0.24 [0.13; 0.31]	8.6 [4.4; 11.9]
GFDL-CM4	2.18 [2.17; 2.19]	2.3 [2.23; 2.37]	−0.14 [−0.18; −0.05]	−6.0 [−7.6; −2.2]
GISS-E2-1-G	1.67 [1.66; 1.68]	1.9 [1.75; 1.92]	−0.2 [−0.26; −0.07]	−10.9 [−13.3; −4.2]
HadGEM3-GC31-LL	2.69 [2.68; 2.71]	2.7 [2.63; 2.82]	−0.04 [−0.12; 0.1]	−1.5 [−4.4; 3.9]
IPSL-CM6A-LR	2.32 [2.29; 2.36]	2.7 [2.53; 2.84]	−0.39 [−0.49; −0.21]	−14.4 [−17.0; −8.2]
MIROC6	1.52 [1.5; 1.54]	1.7 [1.59; 1.77]	−0.19 [−0.24; −0.09]	−11.3 [−13.4; −5.5]
MRI-ESM2-0	1.72 [1.71; 1.73]	1.8 [1.69; 1.8]	−0.04 [−0.09; 0.06]	−2.4 [−4.9; 3.7]
NorESM2-LM	1.53 [1.51; 1.55]	1.7 [1.51; 1.77]	−0.13 [−0.27; 0.01]	−7.6 [−15.1; 0.4]
Mean	2.15 [1.66; 2.66]	2.3 [1.75; 2.78]	−0.14 [−0.28; 0.01]	−6.0 [−11.3; 0.5]

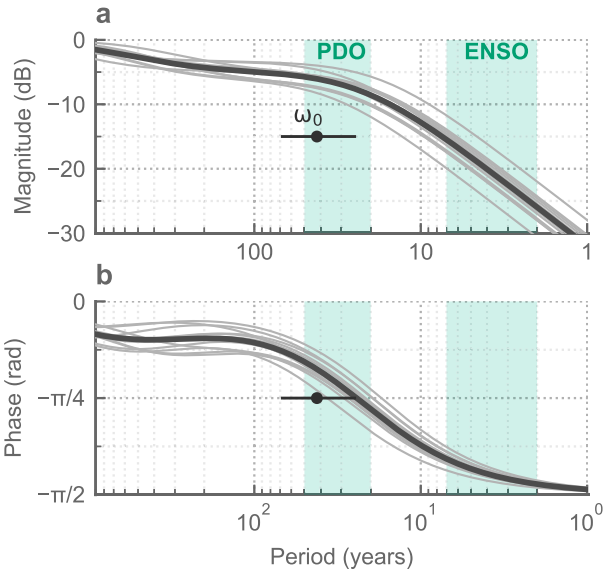

FIG. 7. Bode plot for the low-pass filter corresponding to the two-layer model for each model studied. Individual models are shown in light gray and the multimodel mean is shown in darker gray with thicker lines. The mean and total range of the cutoff frequencies ω_0 are displayed with a gray marker and a gray horizontal line, respectively. Periods roughly corresponding to ENSO and the PDO are indicated with the green shaded areas. (a) Magnitude reduction of the filter. (b) Phase shift of the filter.

CO_2. In this section, we explore these two possibilities with CESM2.

To determine Eq. (2) for the multivariate radiative response, we only used the first-order Taylor expansion. However, several studies (e.g., Bloch-Johnson et al. 2021; Ceppi and Gregory 2019) suggest that models show a feedback temperature dependence that becomes significant for a high GMST change. Regardless of changing patterns, this would mean that the radiative response to uniform warming is not linear but quadratic with the GMST change. With this additional quadratic dependence, the Earth energy imbalance [Eq. (3)] would read

$$N(t) = F(t) + \lambda_1 \overline{T}(t) + \lambda_2 \overline{T}^2(t) + P(t). \quad (15)$$

Bloch-Johnson et al. (2021) show that CESM2 has one of the highest feedback temperature dependences of the 14 models they studied. To test the influence of the feedback temperature dependence on our reconstruction, we use an approximate value of $\lambda_2 = 0.04$ W m^{-2} K^{-2}, which is within the range of Bloch-Johnson et al. (2021). With this, the RMSE between the Earth energy imbalance and the multivariate energy balance approximation for CESM2 goes from 0.43 to 0.39 W m^{-2} and produces a visually better reconstruction (see Fig. S9b).

We assumed that the radiative forcing is logarithmically increasing with time. This approximation is a very good first-order approximation but can be limited (Gregory et al. 2015; Etminan et al. 2016). Notably, Gregory et al. (2015) showed that this approximation could lead to errors in interpreting the GMST change in 1pctCO2 experiments. Instead of using a linear approximation, they parameterize the forcing as

$$F(t) = f_1 t + f_2 t^2. \quad (16)$$

Using ordinary least squares on the CESM2 run, which has the largest errors using Eq. (3), we estimate $f_1 = 0.063$ W m^{-2} yr^{-1} and $f_2 = 7 \times 10^{-5}$ W m^{-2} yr^{-2}, which is consistent with the values found by Gregory et al. (2015). Such estimates of the forcing slightly reduce the RMSE between the true Earth energy imbalance and the multivariate energy balance model from 0.43 to 0.40 W m^{-2}, which is of similar magnitude as if there was a quadratic dependence to the GMST. The fit is also visually better as shown in Fig. S9c.

These two sources of error could explain the differences between the multivariable energy budget [Eq. (3)] and the Earth energy imbalance for the last decades of the simulation. However, determining precisely which one has the most impact here would require further investigation. To accurately quantify these two potential sources of error, one could use specific simulations to determine their individual contributions. The nonlogarithmic forcing of CO_2 could be determined using a piClim-1pctCO$_2$ simulation, which would be a fixed-SST experiment, similar to piClim-4xCO_2, but with gradually increasing CO_2 concentrations. This would be, in essence, similar to piClim-histall experiments from RFMIP (Pincus et al. 2016). The nonlogarithmic forcing would not lead to reconstruction errors with such an explicit estimate of radiative forcing. The feedback temperature dependence for uniform warming could be determined using several uniform warming experiments with various warming levels (amip-p2K, amip-p4K, and amip-p6K) as in Ceppi and Gregory (2019). This way, the quadratic dependence of the radiative response on uniform warming could be estimated. Note that some additional nonlinearities could also arise from the Green functions (Williams et al. 2023; Bloch-Johnson et al. 2024), which would require more elaborate developments to determine the pattern effect. These potential errors have not been quantified in this study.

b. *Relevance for historical and future warming*

In this study, we only looked at an idealized setup to study transient warming. However, key elements are missing to compare our results with historical and future warming. First, we mostly focused on the forced component, while internal variability is more important compared to the forced response in historical or future warming (Meyssignac et al. 2023a; Dessler 2020; Chao et al. 2022). Second, we only looked at the pattern effect induced by CO_2 radiative forcing. However, different forcing agents can induce different pattern effects (Zhou et al. 2023; Salvi et al. 2023), and notably aerosol forcing has been identified as a key driver of warming pattern formation (Hwang et al. 2024; McMonigal 2024; Günther et al. 2022), which is not taken into account in our idealized case.

We now compare our results with the forced components of historical simulations. We compute the pattern effect time

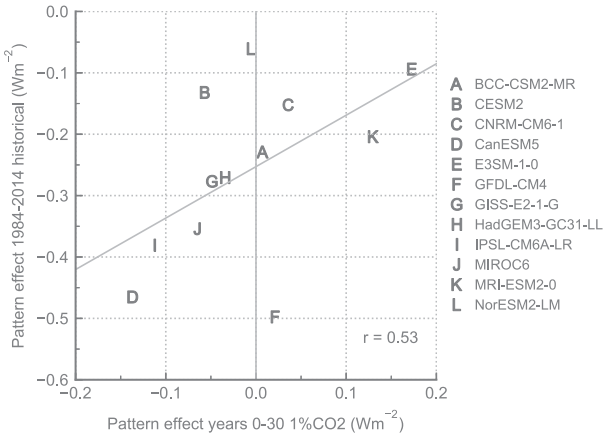

FIG. 8. Comparing the pattern effect in historical simulations and in 1pctCO$_2$ simulations. The letters indicate the mean pattern effect in the first 30 years of the 1pctCO2 simulation (x axis) and the ensemble-mean pattern effect over the years 1984–2014 in historical simulations (y axis) for each model studied. The dashed line shows the regression line between the two variables.

series in historical simulations using the same method as in section 3 and average the results over all ensemble members available for each model to extract only the forced response. The pattern effect time series are presented in Fig. S10. Overall, we find that the forced pattern effect is also generally negative in historical simulations, which would damp global warming as in 1pctCO$_2$ simulations. Figure 8 shows the magnitude of the pattern effect during the first 30 years of the 1pctCO2 simulations compared to the last 30 years of the historical simulations. We find that models that tend to have more negative pattern effects in 1pctCO$_2$ simulations also have more negative pattern effects in historical simulations (with a Pearson r value of 0.53). Although the quantification is limited, this shows that the forced pattern effect in response to CO$_2$ increase is relevant for the forced historical response. Our results suggest that during the historical period, the pattern effect may be generally dominated by CO$_2$ forcing. This is consistent with previous work highlighting that 1pctCO$_2$ and historical simulations have similar patterns of warming (Dong et al. 2021; Armour et al. 2024). Further studies could apply our analysis to separate forcing experiments using RFMIP simulations such as piClim-GHG and piClim-aer.

Figure 8 only shows the forced response comparison. Contrary to 1pctCO$_2$ runs, historical simulations are much more subject to internal variability compared to the forced signal. Our results suggest that high-frequency variability such as ENSO (Ceppi and Gregory 2019; Tsuchida et al. 2023) should not impact the GMST through their pattern effect in historical simulations as it is filtered out by the low-pass filter imposed by the ocean dynamics. However, internal variability associated with the PDO is likely to affect GMST in historical simulations or in the real world. Further study should investigate the influence of low-frequency variability on the pattern effect (e.g., Wills et al. 2021).

Multiple studies highlight that the pattern of warming in historical simulations is different than the pattern in observed SST, which is likely due to the systematic biases in climate models (Seager et al. 2022; Wills et al. 2022). Notable biases in tropical warming gradients have been associated with biases in the global radiative response (e.g., Fueglistaler and Silvers 2021; Andrews et al. 2022; Armour 2017; Chenal et al. 2022). In climate model simulations, the historical warming patterns are close to the 1pctCO$_2$ patterns and both are different from the observed warming patterns, meaning the quantitative impact of the pattern effect on historical warming is likely different from the results shown in this study. As we provide a framework to systematically quantify the impact of the pattern effect on GMST change, our approach could further be applied to understand how the observed warming patterns affected the historical GMST. One could notably determine how such a historical pattern would affect decadal climate projections if it was forced and thus persistent over the decades to come [extending the work from Watanabe et al. (2021), Alessi and Rugenstein (2023); Liang et al. (2024); Armour et al. (2024].

6. Conclusions

In this paper, we have quantified the radiative response to nonuniform warming, referred to as the pattern effect, in 1pctCO$_2$ experiments and determined its influence on decadal global warming. To do so, we separated the radiative response induced by uniform warming from the radiative response induced by changing warming patterns. Overall, we found that in 1pctCO$_2$ experiments, the pattern effect is essentially forced and induces a negative radiative response, which consequently dampens global warming. Notably, we show that the transient climate response is reduced by 6% on average because of the pattern effect. We also found differences in climate models and highlighted that the forced pattern effect can significantly affect decadal warming. Our results are representative of the forced pattern effect in historical simulations, but further work is required to determine the influence of other forcing agents, such as aerosols, and of the modes of atmosphere–ocean internal variability on global warming through the pattern effect. We highlight that the impact on the GMST of the high-frequency variability of the pattern effect, such as associated with ENSO, should be largely attenuated, while the PDO may substantially influence decadal warming.

Acknowledgments. We acknowledge the World Climate Research Programme's Working Group on Coupled Modelling, which is responsible for CMIP, and we thank the climate modeling groups for producing and making available their model output, specifically modeling groups participating in CFMIP and RFMIP. We also thank the GFMIP community for making the preliminary Green's functions outputs available online. We also thank Rémy Roca and Paulo Ceppi for their insightful discussions and comments. The authors declare no conflict of interest. R.G.C was partly funded by the European Union, GA\#101126560; Bergen research and training program for future AI leaders across the disciplines, LEAD AI. B.M. was supported by the ESA Climate space Programme under the Cross-ECV project MOTECUSOMA.

Data availability statement. CMIP6 data used in this study are available on the Earth System Grid Foundation at https://esgf.llnl.gov/. All Green's functions are available at https://github.com/GFMIP/preliminary_spatial_feedbacks/tree/main/data. Surface albedo feedback data are available at https://github.com/mzelinka/cmip56_forcing_feedback_ecs. Snow surface albedo feedback data were extracted from Table 1 of Qu and Hall (2014). Scripts for the processing and figures in this paper are available on the following Zenodo archive: https://zenodo.org/records/15727307 and https://doi.org/10.5281/zenodo.15727306.

APPENDIX A

Mode Parameters for the Two-Layer Ocean Model

Following Geoffroy et al. (2013a) and Rohrschneider et al. (2019), using the two-layer ocean model to represent the ocean inertia yields the following GMST change in response to the change in radiative forcing F and to the pattern P [Eq. (6)]:

$$\begin{cases} \overline{T}_F(t) = \dfrac{1}{C(\psi_s + \psi_f)}\left[\psi_f \displaystyle\int_0^t F(s)e^{-(t-s)/\tau_f}ds + \psi_s \int_0^t F(s)e^{-(t-s)/\tau_f}ds\right] \\ \overline{T}_P(t) = \dfrac{1}{C(\psi_s + \psi_f)}\left[\psi_f \displaystyle\int_0^t P(s)e^{-(t-s)/\tau_f}ds + \psi_s \int_0^t P(s)e^{-(t-s)/\tau_f}ds\right] \end{cases}, \tag{A1}$$

where τ_s and τ_f are the slow and fast characteristic time scales, respectively, and ψ_s and ψ_s are the mode parameters. These four parameters can be obtained by combining the ocean model parameters C, C_0, and γ with the uniform warming climate feedback parameter λ_u with

$$\begin{cases} b = \dfrac{\lambda_u + \gamma}{C} + \dfrac{\gamma}{C_0} \qquad b^* = \dfrac{\lambda_u + \gamma}{C} - \dfrac{\gamma}{C_0} \qquad \delta = b^2 - 4\dfrac{\lambda_u \gamma}{CC_0} \\ \tau_f = \dfrac{CC_0}{2\lambda_u \gamma}(b - \sqrt{\delta}) \qquad \tau_s = \dfrac{CC_0}{2\lambda_u \gamma}(b + \sqrt{\delta}) \\ \psi_f = \dfrac{C}{2\gamma}(b^* - \sqrt{\delta}) \qquad \psi_s = \dfrac{C}{2\gamma}(b^* + \sqrt{\delta}) \end{cases}. \tag{A2}$$

More details on how to determine these parameters are provided in Geoffroy et al. (2013a) and Rohrschneider et al. (2019).

APPENDIX B

Quantifying the Sea Ice Surface Albedo Feedback

While the data for α_{ice} are not directly available for the models we are using, we can estimate it using the values from the total surface albedo feedback quantified by Zelinka et al. (2020), which were computed using radiative kernels. The total surface albedo feedback is primarily driven by the changes in sea ice and snow cover (IPCC 2021). Thus, we can express the total surface albedo feedback α as the sum of contributions from snow, here α_{snow} and ice: $\alpha = \alpha_{snow} + \alpha_{ice}$.

We assume that the ratio of α_{ice} to the total surface albedo feedback α is consistent across different climate models. We then compute this ratio using CMIP5 model data, combining Zelinka et al. (2020) estimates of total surface albedo feedback α and snow surface albedo feedback estimates α_{snow} from Qu and Hall (2014). Our findings suggest an $\alpha_{ice}/\alpha_{tot}$ ratio of 0.82 ± 0.06 for CMIP5 models. This consistency across models supports our hypothesis that the ratio of α_{ice} to the total surface albedo feedback is relatively stable.

This ratio is then combined with each individual CMIP6 model's α estimate from Zelinka et al. (2020). We estimate the sea ice surface albedo feedback to be 0.37 ± 0.08 W m^{-1} K^{-1} (multimodel mean and standard deviation), which is slightly higher than the values used by Ceppi and Gregory (2019), of 0.20 and 0.30 W m^{-2} K^{-1}.

REFERENCES

Ackerley, D., R. Chadwick, D. Dommenget, and P. Petrelli, 2018: An ensemble of AMIP simulations with prescribed land surface temperatures. *Geosci. Model Dev.*, **11**, 3865–3881, https://doi.org/10.5194/gmd-11-3865-2018.

Alessi, M. J., and M. A. A. Rugenstein, 2023: Surface temperature pattern scenarios suggest higher warming rates than current projections. *Geophys. Res. Lett.*, **50**, e2023GL105795, https://doi.org/10.1029/2023GL105795.

Andrews, T., and M. J. Webb, 2018: The dependence of global cloud and lapse rate feedbacks on the spatial structure of tropical Pacific warming. *J. Climate*, **31**, 641–654, https://doi.org/10.1175/JCLI-D-17-0087.1.

——, J. M. Gregory, and M. J. Webb, 2015: The dependence of radiative forcing and feedback on evolving patterns of surface temperature change in climate models. *J. Climate*, **28**, 1630–1648, https://doi.org/10.1175/JCLI-D-14-00545.1.

——, and Coauthors, 2018: Accounting for changing temperature patterns increases historical estimates of climate sensitivity. *Geophys. Res. Lett.*, **45**, 8490–8499, https://doi.org/10.1029/2018GL078887.

——, C. J. Smith, G. Myhre, P. M. Forster, R. Chadwick, and D. Ackerley, 2021: Effective radiative forcing in a GCM with fixed surface temperatures. *J. Geophys. Res. Atmos.*, **126**, e2020JD033880, https://doi.org/10.1029/2020JD033880.

——, and Coauthors, 2022: On the effect of historical SST patterns on radiative feedback. *J. Geophys. Res. Atmos.*, **127**, e2022JD036675, https://doi.org/10.1029/2022JD036675.

Archer, D., and R. Pierrehumbert, 2011: *The Warming Papers: The Scientific Foundation for the Climate Change Forecast.* John Wiley and Sons, 432 pp.

Armour, K. C., 2017: Energy budget constraints on climate sensitivity in light of inconstant climate feedbacks. *Nat. Climate Change*, **7**, 331–335, https://doi.org/10.1038/nclimate3278.

——, C. M. Bitz, and G. H. Roe, 2013: Time-varying climate sensitivity from regional feedbacks. *J. Climate*, **26**, 4518–4534, https://doi.org/10.1175/JCLI-D-12-00544.1.

——, and Coauthors, 2024: Sea-surface temperature pattern effects have slowed global warming and biased warming-based constraints on climate sensitivity. *Proc. Natl. Acad. Sci. USA*, **121**, e2312093121, https://doi.org/10.1073/pnas.2312093121.

Barsugli, J. J., and P. D. Sardeshmukh, 2002: Global atmospheric sensitivity to tropical SST anomalies throughout the Indo-

Pacific basin. *J. Climate*, **15**, 3427–3442, https://doi.org/10.1175/1520-0442(2002)015<3427:GASTTS>2.0.CO;2.

Bloch-Johnson, J., M. A. A. Rugenstein, M. B. Stolpe, T. Rohrschneider, Y. Zheng, and J. M. Gregory, 2021: Climate sensitivity increases under higher CO_2 levels due to feedback temperature dependence. *Geophys. Res. Lett.*, **48**, e2020GL089074, https://doi.org/10.1029/2020GL089074.

——, and Coauthors, 2024: The Green's Function Model Intercomparison Project (GFMIP). *J. Adv. Model. Earth Syst.*, **16**, e2023MS003700, https://doi.org/10.1029/2023MS003700.

Boucher, O., and Coauthors, 2020: Presentation and evaluation of the IPSL-CM6A-LR climate model. *J. Adv. Model. Earth Syst.*, **12**, e2019MS002010, https://doi.org/10.1029/2019MS002010.

Budyko, M. I., 1969: The effect of solar radiation variations on the climate of the Earth. *Tellus*, **21** (5), 611–619, https://doi.org/10.1111/j.2153-3490.1969.tb00466.x.

Ceppi, P., and J. M. Gregory, 2017: Relationship of tropospheric stability to climate sensitivity and Earth's observed radiation budget. *Proc. Natl. Acad. Sci. USA*, **114**, 13 126–13 131, https://doi.org/10.1073/pnas.1714308114.

——, and ——, 2019: A refined model for the Earth's global energy balance. *Climate Dyn.*, **53**, 4781–4797, https://doi.org/10.1007/s00382-019-04825-x.

——, and S. Fueglistaler, 2021: The El Niño–Southern Oscillation pattern effect. *Geophys. Res. Lett.*, **48**, e2021GL095261, https://doi.org/10.1029/2021GL095261.

Cess, R. D., and Coauthors, 1990: Intercomparison and interpretation of climate feedback processes in 19 atmospheric general circulation models. *J. Geophys. Res.*, **95**, 16 601–16 615, https://doi.org/10.1029/JD095iD10p16601.

Chao, L.-W., J. C. Muller, and A. E. Dessler, 2022: Impacts of the unforced pattern effect on the cloud feedback in CERES observations and climate models. *Geophys. Res. Lett.*, **49**, e2021GL096299, https://doi.org/10.1029/2021GL096299.

Chenal, J., B. Meyssignac, A. Ribes, and R. Guillaume-Castel, 2022: Observational constraint on the climate sensitivity to atmospheric CO_2 concentrations changes derived from the 1971–2017 global energy budget. *J. Climate*, **35**, 4469–4483, https://doi.org/10.1175/JCLI-D-21-0565.1.

Danabasoglu, G., and Coauthors, 2020: The Community Earth System Model version 2 (CESM2). *J. Adv. Model. Earth Syst.*, **12**, e2019MS001916, https://doi.org/10.1029/2019MS001916.

Dessler, A. E., 2020: Potential problems measuring climate sensitivity from the historical record. *J. Climate*, **33**, 2237–2248, https://doi.org/10.1175/JCLI-D-19-0476.1.

Dickinson, R. E., 1981: Convergence rate and stability of ocean-atmosphere coupling schemes with a zero-dimensional climate model. *J. Atmos. Sci.*, **38**, 2112–2120, https://doi.org/10.1175/1520-0469(1981)038<2112:CRASOO>2.0.CO;2.

Dong, Y., C. Proistosescu, K. C. Armour, and D. S. Battisti, 2019: Attributing historical and future evolution of radiative feedbacks to regional warming patterns using a Green's function approach: The preeminence of the western Pacific. *J. Climate*, **32**, 5471–5491, https://doi.org/10.1175/JCLI-D-18-0843.1.

——, and Coauthors, 2021: Biased estimates of equilibrium climate sensitivity and transient climate response derived from historical CMIP6 simulations. *Geophys. Res. Lett.*, **48**, e2021GL095778, https://doi.org/10.1029/2021GL095778.

——, A. G. Pauling, S. Sadai, and K. C. Armour, 2022: Antarctic ice-sheet meltwater reduces transient warming and climate sensitivity through the sea-surface temperature pattern effect. *Geophys. Res. Lett.*, **49**, e2022GL101249, https://doi.org/10.1029/2022GL101249.

Dunne, J. P., and Coauthors, 2020: The GFDL Earth System Model version 4.1 (GFDL-ESM 4.1): Overall coupled model description and simulation characteristics. *J. Adv. Model. Earth Syst.*, **12**, e2019MS002015, https://doi.org/10.1029/2019MS002015.

Etminan, M., G. Myhre, E. J. Highwood, and K. P. Shine, 2016: Radiative forcing of carbon dioxide, methane, and nitrous oxide: A significant revision of the methane radiative forcing. *Geophys. Res. Lett.*, **43**, 12 614–12 623, https://doi.org/10.1002/2016GL071930.

Eyring, V., S. Bony, G. A. Meehl, C. A. Senior, B. Stevens, R. J. Stouffer, and K. E. Taylor, 2016: Overview of the Coupled Model Intercomparison Project Phase 6 (CMIP6) experimental design and organization. *Geosci. Model Dev.*, **9**, 1937–1958, https://doi.org/10.5194/gmd-9-1937-2016.

E3SM Project, 2018: Energy exascale Earth system model v1.0. https://e3sm.org/.

Forster, P. M., and Coauthors, 2016: Recommendations for diagnosing effective radiative forcing from climate models for CMIP6. *J. Geophys. Res. Atmos.*, **121**, 12 460–12 475, https://doi.org/10.1002/2016JD025320.

Frey, W. R., E. A. Maroon, A. G. Pendergrass, and J. E. Kay, 2017: Do Southern ocean cloud feedbacks matter for 21st century warming? *Geophys. Res. Lett.*, **44**, 12 447–12 456, https://doi.org/10.1002/2017GL076339.

Fueglistaler, S., 2019: Observational evidence for two modes of coupling between sea surface temperatures, tropospheric temperature profile, and shortwave cloud radiative effect in the tropics. *Geophys. Res. Lett.*, **46**, 9890–9898, https://doi.org/10.1029/2019GL083990.

——, and L. G. Silvers, 2021: The peculiar trajectory of global warming. *J. Geophys. Res. Atmos.*, **126**, e2020JD033629, https://doi.org/10.1029/2020JD033629.

Geoffroy, O., D. Saint-Martin, and A. Ribes, 2012: Quantifying the sources of spread in climate change experiments. *Geophys. Res. Lett.*, **39**, L24703, https://doi.org/10.1029/2012GL054172.

——, ——, D. J. L. Olivié, A. Voldoire, G. Bellon, and S. Tytéca, 2013a: Transient climate response in a two-layer energy-balance model. Part I: Analytical solution and parameter calibration using CMIP5 AOGCM experiments. *J. Climate*, **26**, 1841–1857, https://doi.org/10.1175/JCLI-D-12-00195.1.

——, ——, G. Bellon, A. Voldoire, D. J. L. Olivié, and S. Tytéca, 2013b: Transient climate response in a two-layer energy-balance model. Part II: Representation of the efficacy of deep-ocean heat uptake and validation for CMIP5 AOGCMs. *J. Climate*, **26**, 1859–1876, https://doi.org/10.1175/JCLI-D-12-00196.1.

Gordon, C., C. Cooper, C. A. Senior, H. Banks, J. M. Gregory, T. C. Johns, J. F. B. Mitchell, and R. A. Wood, 2000: The simulation of SST, sea ice extents and ocean heat transports in a version of the Hadley Centre coupled model without flux adjustments. *Climate Dyn.*, **16**, 147–168, https://doi.org/10.1007/s003820050010.

Gregory, J. M., 2000: Vertical heat transports in the ocean and their effect on time-dependent climate change. *Climate Dyn.*, **16**, 501–515, https://doi.org/10.1007/s003820000059.

——, T. Andrews, and P. Good, 2015: The inconstancy of the transient climate response parameter under increasing CO_2. *Philos. Trans. Roy. Soc.*, **A373**, 20140417, https://doi.org/10.1098/rsta.2014.0417.

——, ——, P. Ceppi, T. Mauritsen, and M. J. Webb, 2020: How accurately can the climate sensitivity to CO_2 be estimated from historical climate change? *Climate Dyn.*, **54**, 129–157, https://doi.org/10.1007/s00382-019-04991-y.

Grose, M. R., R. Colman, J. Bhend, and A. F. Moise, 2017: Limits to global and Australian temperature change this century based on expert judgment of climate sensitivity. *Climate Dyn.*, **48**, 3325–3339, https://doi.org/10.1007/s00382-016-3269-2.

——, J. Gregory, R. Colman, and T. Andrews, 2018: What climate sensitivity index is most useful for projections? *Geophys. Res. Lett.*, **45**, 1559–1566, https://doi.org/10.1002/2017GL075742.

Günther, M., H. Schmidt, C. Timmreck, and M. Toohey, 2022: Climate feedback to stratospheric aerosol forcing: The key role of the pattern effect. *J. Climate*, **35**, 7903–7917, https://doi.org/10.1175/JCLI-D-22-0306.1.

Hansen, J., and Coauthors, 2005: Efficacy of climate forcings. *J. Geophys. Res.*, **110**, D18104, https://doi.org/10.1029/2005JD005776.

Held, I. M., M. Winton, K. Takahashi, T. Delworth, F. Zeng, and G. K. Vallis, 2010: Probing the fast and slow components of global warming by returning abruptly to preindustrial forcing. *J. Climate*, **23**, 2418–2427, https://doi.org/10.1175/2009JCLI3466.1.

Hwang, Y.-T., S.-P. Xie, P.-J. Chen, H.-Y. Tseng, and C. Deser, 2024: Contribution of anthropogenic aerosols to persistent La Niña-like conditions in the early 21st century. *Proc. Natl. Acad. Sci. USA*, **121**, e2315124121, https://doi.org/10.1073/pnas.2315124121.

IPCC, 2021: The Earth's energy budget, climate feedbacks and climate sensitivity. *Climate Change 2021: The Physical Science Basis*, V. Masson-Delmotte et al., Eds., Cambridge University Press, 923–1054, https://doi.org/10.1017/9781009157896.009.

Kelley, M., and Coauthors, 2020: GISS-E2.1: Configurations and climatology. *J. Adv. Model. Earth Syst.*, **12**, e2019MS002025, https://doi.org/10.1029/2019MS002025.

Liang, Y., N. P. Gillett, and A. H. Monahan, 2024: Accounting for Pacific climate variability increases projected global warming. *Nat. Climate Change*, **14**, 608–614, https://doi.org/10.1038/s41558-024-02017-y.

Loeb, N. G., T. J. Thorsen, J. R. Norris, H. Wang, and W. Su, 2018: Changes in Earth's energy budget during and after the "pause" in global warming: An observational perspective. *Climate*, **6**, 62, https://doi.org/10.3390/cli6030062.

Marvel, K., R. Pincus, G. A. Schmidt, and R. L. Miller, 2018: Internal variability and disequilibrium confound estimates of climate sensitivity from observations. *Geophys. Res. Lett.*, **45**, 1595–1601, https://doi.org/10.1002/2017GL076468.

McMonigal, K., 2024: Aerosols hold the key to recent and future Pacific warming patterns. *Proc. Natl. Acad. Sci. USA*, **121**, e2322594121, https://doi.org/10.1073/pnas.2322594121.

Meyssignac, B., J. Chenal, N. Loeb, R. Guillaume-Castel, and A. Ribes, 2023a: Time-variations of the climate feedback parameter λ are associated with the Pacific Decadal Oscillation. *Commun. Earth Environ.*, **4**, 241, https://doi.org/10.1038/s43247-023-00887-2.

——, R. Guillaume-Castel, and R. Roca, 2023b: Revisiting the global energy budget dynamics with a multivariate Earth energy balance model to account for the warming pattern effect. *J. Climate*, **36**, 8113–8126, https://doi.org/10.1175/JCLI-D-22-0765.1.

Mitchell, T. D., 2003: Pattern scaling: An examination of the accuracy of the technique for describing future climates. *Climatic Change*, **60**, 217–242, https://doi.org/10.1023/A:1026035305597.

Myhre, G., E. J. Highwood, K. P. Shine, and F. Stordal, 1998: New estimates of radiative forcing due to well mixed greenhouse gases. *Geophys. Res. Lett.*, **25**, 2715–2718, https://doi.org/10.1029/98GL01908.

Neale, R. B., and Coauthors, 2010: Description of the NCAR Community Atmosphere Model (CAM 5.0). NCAR Tech. Note NCAR/TN-486+STR, 268 pp., www.cesm.ucar.edu/models/cesm1.1/cam/docs/description/cam5_desc.pdf.

——, J. Richter, S. Park, P. H. Lauritzen, S. J. Vavrus, P. J. Rasch, and M. Zhang, 2013: The mean climate of the Community Atmosphere Model (CAM4) in forced SST and fully coupled experiments. *J. Climate*, **26**, 5150–5168, https://doi.org/10.1175/JCLI-D-12-00236.1.

North, G. R., and K.-Y. Kim, 2017: *Energy Balance Climate Models.* John Wiley and Sons, 392 pp.

Perrette, M., F. Landerer, R. Riva, K. Frieler, and M. Meinshausen, 2013: A scaling approach to project regional sea level rise and its uncertainties. *Earth Syst. Dyn.*, **4**, 11–29, https://doi.org/10.5194/esd-4-11-2013.

Pincus, R., P. M. Forster, and B. Stevens, 2016: The Radiative Forcing Model Intercomparison Project (RFMIP): Experimental protocol for CMIP6. *Geosci. Model Dev.*, **9**, 3447–3460, https://doi.org/10.5194/gmd-9-3447-2016.

Qu, X., and A. Hall, 2014: On the persistent spread in snow-albedo feedback. *Climate Dyn.*, **42**, 69–81, https://doi.org/10.1007/s00382-013-1774-0.

Raper, S. C. B., J. M. Gregory, and R. J. Stouffer, 2002: The role of climate sensitivity and ocean heat uptake on AOGCM transient temperature response. *J. Climate*, **15**, 124–130, https://doi.org/10.1175/1520-0442(2002)015<0124:TROCSA>2.0.CO;2.

Ringer, M. A., A. Bodas-Salcedo, and M. J. Webb, 2023: Global and regional climate feedbacks in response to uniform warming and cooling. *J. Geophys. Res. Atmos.*, **128**, e2023JD038861, https://doi.org/10.1029/2023JD038861.

Rohrschneider, T., B. Stevens, and T. Mauritsen, 2019: On simple representations of the climate response to external radiative forcing. *Climate Dyn.*, **53**, 3131–3145, https://doi.org/10.1007/s00382-019-04686-4.

Romps, D. M., J. T. Seeley, and J. P. Edman, 2022: Why the forcing from carbon dioxide scales as the logarithm of its concentration. *J. Climate*, **35**, 4027–4047, https://doi.org/10.1175/JCLI-D-21-0275.1.

Salvi, P., J. M. Gregory, and P. Ceppi, 2023: Time-evolving radiative feedbacks in the historical period. *J. Geophys. Res. Atmos.*, **128**, e2023JD038984, https://doi.org/10.1029/2023JD038984.

Santer, B. D., T. M. L. Wigley, M. E. Schlesinger, and J. F. B. Mitchell, 1990: Developing climate scenarios from equilibrium GCM results. Max-Planck-Institut für Meteorologie Rep. 47, 31 pp., https://pure.mpg.de/rest/items/item_2566446/component/file_2566445/content.

Schiro, K. A., and Coauthors, 2022: Model spread in tropical low cloud feedback tied to overturning circulation response to warming. *Nat. Commun.*, **13**, 7119, https://doi.org/10.1038/s41467-022-34787-4.

Seager, R., N. Henderson, and M. Cane, 2022: Persistent discrepancies between observed and modeled trends in the tropical Pacific Ocean. *J. Climate*, **35**, 4571–4584, https://doi.org/10.1175/JCLI-D-21-0648.1.

Seland, Ø., and Coauthors, 2020: Overview of the Norwegian Earth System Model (NorESM2) and key climate response of CMIP6 DECK, historical, and scenario simulations. *Geosci. Model Dev.*, **13**, 6165–6200, https://doi.org/10.5194/gmd-13-6165-2020.

Sellers, W. D., 1969: A global climatic model based on the energy balance of the Earth-atmosphere system. *J. Appl. Meteor.*, **8**, 392–400, https://doi.org/10.1175/1520-0450(1969)008<0392:AGCMBO>2.0.CO;2.

Sherwood, S. C., and Coauthors, 2020: An assessment of Earth's climate sensitivity using multiple lines of evidence. *Rev. Geophys.*, **58**, e2019RG000678, https://doi.org/10.1029/2019RG000678.

Smith, C. J., and Coauthors, 2018: Understanding rapid adjustments to diverse forcing agents. *Geophys. Res. Lett.*, **45**, 12 023–12 031, https://doi.org/10.1029/2018GL079826.

——, Z. R. J. Nicholls, K. Armour, W. Collins, P. M. Forster, M. Meinshausen, M. D. Palmer, and M. Watanabe, 2021: The Earth's energy budget, climate feedbacks and climate sensitivity supplementary material. *Climate Change 2021: The Physical Science Basis*, V. Masson-Delmotte et al., Eds., Cambridge University Press, 1850–2005.

Stevens, B., and Coauthors, 2013: Atmospheric component of the MPI-M Earth system model: ECHAM6. *J. Adv. Model. Earth Syst.*, **5**, 146–172, https://doi.org/10.1002/jame.20015.

——, S. C. Sherwood, S. Bony, and M. J. Webb, 2016: Prospects for narrowing bounds on Earth's equilibrium climate sensitivity. *Earth's Future*, **4**, 512–522, https://doi.org/10.1002/2016EF000376.

Swart, N. C., and Coauthors, 2019: The Canadian Earth System Model version 5 (CanESM5.0.3). *Geosci. Model Dev.*, **12**, 4823–4873, https://doi.org/10.5194/gmd-12-4823-2019.

Tatebe, H., and Coauthors, 2019: Description and basic evaluation of simulated mean state, internal variability, and climate sensitivity in MIROC6. *Geosci. Model Dev.*, **12**, 2727–2765, https://doi.org/10.5194/gmd-12-2727-2019.

Tsuchida, K., T. Mochizuki, R. Kawamura, and T. Kawano, 2023: Interdecadal variations of radiative feedbacks associated with the El Niño and Southern Oscillation (ENSO) in CMIP6 models. *Geophys. Res. Lett.*, **50**, e2023GL106127, https://doi.org/10.1029/2023GL106127.

Voldoire, A., and Coauthors, 2019: Evaluation of CMIP6 DECK experiments with CNRM-CM6-1. *J. Adv. Model. Earth Syst.*, **11**, 2177–2213, https://doi.org/10.1029/2019MS001683.

Watanabe, M., J.-L. Dufresne, Y. Kosaka, T. Mauritsen, and H. Tatebe, 2021: Enhanced warming constrained by past trends in equatorial Pacific sea surface temperature gradient. *Nat. Climate Change*, **11**, 33–37, https://doi.org/10.1038/s41558-020-00933-3.

Webb, M. J., and Coauthors, 2017: The Cloud Feedback Model Intercomparison Project (CFMIP) contribution to CMIP6. *Geosci. Model Dev.*, **10**, 359–384, https://doi.org/10.5194/gmd-10-359-2017.

Williams, A. I. L., N. Jeevanjee, and J. Bloch-Johnson, 2023: Circus tents, convective thresholds, and the non-linear climate response to tropical SSTs. *Geophys. Res. Lett.*, **50**, e2022GL101499, https://doi.org/10.1029/2022GL101499.

Williams, K. D., and Coauthors, 2018: The Met Office Global Coupled Model 3.0 and 3.1 (GC3.0 and GC3.1) configurations. *J. Adv. Model. Earth Syst.*, **10**, 357–380, https://doi.org/10.1002/2017MS001115.

Wills, R. C. J., K. C. Armour, D. S. Battisti, C. Proistosescu, and L. A. Parsons, 2021: Slow modes of global temperature variability and their impact on climate sensitivity estimates. *J. Climate*, **34**, 8717–8738, https://doi.org/10.1175/JCLI-D-20-1013.1.

——, Y. Dong, C. Proistosecu, K. C. Armour, and D. S. Battisti, 2022: Systematic climate model biases in the large-scale patterns of recent sea-surface temperature and sea-level pressure change. *Geophys. Res. Lett.*, **49**, e2022GL100011, https://doi.org/10.1029/2022GL100011.

Winton, M., K. Takahashi, and I. M. Held, 2010: Importance of ocean heat uptake efficacy to transient climate change. *J. Climate*, **23**, 2333–2344, https://doi.org/10.1175/2009JCLI3139.1.

——, S. M. Griffies, B. L. Samuels, J. L. Sarmiento, and T. L. Frölicher, 2013: Connecting changing ocean circulation with changing climate. *J. Climate*, **26**, 2268–2278, https://doi.org/10.1175/JCLI-D-12-00296.1.

Wu, T., and Coauthors, 2019: The Beijing Climate Center Climate System Model (BCC-CSM): The main progress from CMIP5 to CMIP6. *Geosci. Model Dev.*, **12**, 1573–1600, https://doi.org/10.5194/gmd-12-1573-2019.

Yukimoto, S., and Coauthors, 2019: The Meteorological Research Institute Earth System Model version 2.0, MRI-ESM2.0: Description and basic evaluation of the physical component. *J. Meteor. Soc. Japan*, **97**, 931–965, https://doi.org/10.2151/jmsj.2019-051.

Zelinka, M. D., T. A. Myers, D. T. McCoy, S. Po-Chedley, P. M. Caldwell, P. Ceppi, S. A. Klein, and K. E. Taylor, 2020: Causes of higher climate sensitivity in CMIP6 models. *Geophys. Res. Lett.*, **47**, e2019GL085782, https://doi.org/10.1029/2019GL085782.

Zhang, B., M. Zhao, and Z. Tan, 2023: Using a Green's function approach to diagnose the pattern effect in GFDL AM4 and CM4. *J. Climate*, **36**, 1105–1124, https://doi.org/10.1175/JCLI-D-22-0024.1.

Zhao, M., and Coauthors, 2018: The GFDL global atmosphere and land model AM4.0/LM4.0: 2. model description, sensitivity studies, and tuning strategies. *J. Adv. Model. Earth Syst.*, **10**, 735–769, https://doi.org/10.1002/2017MS001209.

Zhou, C., M. D. Zelinka, and S. A. Klein, 2016: Impact of decadal cloud variations on the Earth's energy budget. *Nat. Geosci.*, **9**, 871–874, https://doi.org/10.1038/ngeo2828.

——, ——, and ——, 2017: Analyzing the dependence of global cloud feedback on the spatial pattern of sea surface temperature change with a Green's function approach. *J. Adv. Model. Earth Syst.*, **9**, 2174–2189, https://doi.org/10.1002/2017MS001096.

——, ——, A. E. Dessler, and M. Wang, 2021: Greater committed warming after accounting for the pattern effect. *Nat. Climate Change*, **11**, 132–136, https://doi.org/10.1038/s41558-020-00955-x.

——, M. Wang, M. D. Zelinka, Y. Liu, Y. Dong, and K. C. Armour, 2023: Explaining forcing efficacy with pattern effect and state dependence. *Geophys. Res. Lett.*, **50**, e2022GL101700, https://doi.org/10.1029/2022GL101700.